Clays Clay Miner.,Vol. 70, No. 5:753–779, 2022
https://doi.org/10.1007/s42860-022-00214-4

ORIGINAL PAPER

Comparison of Epithermal Kaolin Deposits from the Etili Area (Çanakkale, Turkey): Mineralogical, Geochemical, and Isotopic Characteristics

Hatice Ünal Ercan · Ö. Işık Ece · Emin Çiftçi · Ayça Aydın

Accepted: 22 November 2022 / Published online: 21 December 2022

Abstract Hydrothermal solutions related to magmatic intrusions that occurred during the Oligo-Miocene resulted in advanced multi-stage alterations and, to varying degrees, kaolinization over a wide area of the Biga Peninsula. The most important formations in these kaolin deposits occurred along the NE–SW-trending Çan-Etili-Bayramiç fault zone. The Bahadırlı, Duman, and Çaltıkara quarries are well preserved kaolin deposits throughout these fault zones located within the Çan Volcanics. Mineralogical, geochemical, and isotopic analyses were performed to identify the environments of formation of kaolins and the origin of the hydrothermal solution that led to the formation of these deposits.

The mineralogical assemblages of each of the quarries differ from each other. The Bahadırlı kaolin quarry comprises kaolinite + alunite ± quartz ± smectite ± plagioclase ± K-feldspar. The Çaltıkara kaolin deposits consist of kaolinite + quartz + alunite ± iron-oxide and ore minerals. The Duman kaolin quarry was considered in two different slopes as a hanging wall block and a footwall block, and the blocks contain kaolinite + quartz + plagioclase ± smectite and kaolinite ± alunite ± smectite ± quartz ± plagioclase ± K-Feldspar ± gypsum, respectively. During petrographic investigations, it was observed that kaolinization occurred generally in K-feldspar and plagioclase phenocrysts and partially in the matrix. Mineralogical and micromorphological investigations revealed that the kaolin group includes the dioctahedral minerals kaolinite and halloysite. According to the trace element contents of the kaolinites, the Çaltıkara and Bahadırlı deposits had a hypogene origin, while the Duman deposit had a supergene origin. $\delta^{18}O$ isotopic values of kaolinites ranged from +10.3 to +18.3‰. $\delta^{34}S$ isotopic values ranged from –17.2 to +20.2‰ of alunite, galena, and pyrite minerals, which indicate different formation environments for the kaolin quarries. $^{40}Ar/^{39}Ar$ dating of alunite revealed that the timing of acid-sulfate alteration was compatible with the magmatic intrusions. All these data revealed the mineralogical, chemical, and isotopic differences caused by the effect of different hydrothermal processes in three kaolin deposits located on the same fault zone, close to each other and similar in age.

Associate Editor: Selahattin Kadir.

Supplementary Information The online version contains supplementary material available at https://doi.org/10.1007/s42860-022-00214-4.

H. Ü. Ercan (✉)
Chemistry and Chemical Processing Technologies, Konya Technical University, Konya, Turkey
e-mail: hunalercan@ktun.edu.tr

Ö. I. Ece · E. Çiftçi · A. Aydın
Faculty of Mines, Istanbul Technical University, Maslak 34469 Istanbul, Turkey

Ö. I. Ece
Department of Geology, University of Georgia, Athens, GA 30602-2501, USA

Keywords Alunite · Hydrothermal alteration · Kaolinite · Silica sinter · Stable isotopes

Introduction

Epithermal systems generally occur some distance from a magmatic intrusion; they are mostly produced by intrusions located ~5–6 km below the surface. Epithermal systems can also occur in areas without volcanic activity or volcanic rocks, however (Hedenquist et al., 2000). Known epithermal systems, defined by their characteristic textures and mineral assemblages, are intrusion-related hydrothermal systems below the paleowater table, ranging in depth from 50 to 1000 m, which formed mostly in subaerial volcanic arcs at upper crustal levels which are observed at temperatures of ~50 to 300°C, the maximum temperature limited by the vapor pressure of boiling water (Cooke & Simmons, 2000; Hedenquist et al. 2000; Lindgren, 1933; Sillitoe et al., 1996; Simon et al., 2005; Wade et al., 2014). Defined epithermal environments are mostly shallow and can host deposits of Au, Ag, and base metals that have also been exploited for a wide range of metals and minerals, including Hg, Sb, Pb, Zn, Cu, Mo, S, halloysite, kaolinite, alunite, and silica (Hedenquist et al. 2000). Volcanic-hydrothermal systems have distinctly different types; these are known as low-sulfidation and high-sulfidation and these reflect the two end-members of the sulfidation states deduced from the sulfide mineral assemblages (Skinner & Barton, 1973). These two end-member styles of deposit can be distinguished easily based on their hypogene and supergene alteration mineralogy. Kaolin is the most observed mineral group in these alteration processes. If primary kaolin deposits are formed by in situ weathering from granitic, siliceous volcanic, and pegmatitic rocks, however, they may have a supergene origin. If they are formed by hydrothermal activities, they may have hypogene deposits, depending on the origin of the hydrothermal solutions; in some cases, a combination of these two processes may occur (Murray & Keller, 1993). According to Dill (2016), supergene kaolin mineralization is often homogeneous and is characterized by oxidized minerals, whereas hypogene kaolin typically has variegated mineralogy with reducing minerals.

The Biga Peninsula, northwest Turkey, is well known for its low- to high-sulfidation ore deposits in which many hydrothermal activities were widely developed (Ağdemir et al., 1994; Çiçek et al., 2021; Ece & Schroeder, 2007; Ece et al., 2008; Ercan et al., 2016; Oyman, 2010; Pirajno, 1995; Yiğit, 2012). Much epithermal mineralization including ore minerals, as well as industrial minerals used in the ceramic and cement industries, in different amounts and chemical compositions, was observed in the region. All these mineral associations are the products of acid-sulfate and alkaline fluids of the epithermal system widely developed in the region (Ercan et al., 2016; Laçin et al., 2021; Oyman, 2019; Yiğit, 2012).

In this region, which has many characteristic features of hydrothermal alteration processes, numerous epithermal mineralizations have occurred along active fault zones. Some of the deposits of the region such as the Sarıbeyli-Sığırlı, Bodurlar, Hamamtepe, Muratlar, and Tepeköy quarries in this site were studied and the mineralogical structures of fossil epithermal sites were revealed, their structural differences were characterized, and origins have been interpreted. All these studies focused firstly on acid-sulfate fluids related to advanced argillic alteration mineral assemblages (Ercan et al., 2016) and also alkaline-chloride fluids related to silica sinters (Ercan et al., 2022). Thus, attempts have been made to reveal the temporal and spatial changes that the region has undergone from the past to the nearly present in relation to hydrothermal solutions.

The Bahadırlı Kaolin Deposit (BKD), the Duman Kaolin Deposit (DKD), and the Çaltıkara Kaolin Deposit (CKD) are found throughout the Çan-Etili-Bayramiç fault zone in the Biga Peninsula and where kaolinization is intensely developed. These quarries are located approximately halfway between the Sarıbeyli-Sığırlı and Bodurlar kaolin quarries in the north and the Hamamtepe and the Muratlar silica quarries in the south, where siliceous and silicified rocks are found. Identifying the mineralogy, determining the lithological features, and interpreting the environments of formation, based on geochemical and isotopic data of these quarries, has helped to reveal the hydrothermal alteration processes in the region.

The present study aimed to reveal the temporal evolution of the alteration zones in the Etili fault zone, and thus make a detailed investigation of the kaolinite deposits produced from acidic solutions. For this purpose, lithological, mineralogical, and

https://doi.org/10.1007/s42860-022-00214-4 Published online by Cambridge University Press

geochemical studies including stable isotopic analyses and age dating were carried out. In addition, biological activity with acid sulfate-rich fluids also was assumed to be effective in the alteration processes of these deposits and, also in support of this hypothesis, micro-morphological images and stable isotopic data were interpreted together.

Geological Characteristics of the Region

Western Turkey is a post-collisional magmatic province with various tectonic sub-units which are: the Rhodope Massif, Sakarya Continent, and Anatolid-Torid Block derived by amalgamation along well defined suture zones. The magmatic activity in the region started in the Biga peninsula with granitic intrusions in the Middle Eocene and ended with the production of similar volcanic and magmatic rocks up to the Late Miocene (Aldanmaz et al., 2000; Altunkaynak & Dilek, 2006; Karacık & Yılmaz, 1998). The stratigraphic characteristic of these magmatic rocks changes from calc-alkaline to alkaline and plutonism-dominated to volcanism-dominated type (Altunkaynak & Genç, 2008; Karacık et al., 2008). The Evciler pluton is an important granodiorite located southeast of the study area. Oligocene–Early Miocene aged felsic-type granodiorite is characterized by high-K, calc-alkaline affinity (Aydın, 2019; Ercan et al., 1995; Genç, 1998; Özdamar, 2018; Siyako et al., 1989; Türkdönmez & Bozcu, 2008; Yılmaz & Karacık, 2001). $^{40}Ar/^{39}Ar$ radiometric age data from hornblende and biotite from previous studies were determined to be 25.5 ± 0.1–28.3 ± 0.1 Ma and 21.9 ± 0.1–31.1 ± 1.4 Ma, respectively (Altunkaynak et al., 2012; Birkle & Satir, 1995; Delaloye & Bingol, 2000; Okay & Satir, 2000; Özdamar et al., 2021a). $^{40}Ar/^{39}Ar$ radiometric dating of alunite obtained from the south of this region indicates ages of 5 ± 0.18 to 32.4 ± 1.2 Ma (Ercan et. al., 2022) and is in good agreement with the aforementioned sequence, because the inception of hydrothermal alteration in the region dates back to the Oligocene (Ercan et al., 2016). Hydrothermal alteration in the region developed along the fault zones and one is the Çan-Etili-Bayramiç fault on which several kaolin deposits occur. The Çan-Etili-Bayramiç Fault Zone existed before the North Anatolian Fault Zone (NAF) and merged with the NAF in Plio-Quaternary times to become the western continuum of the southern branch (Kaymakci et al., 2007; Le Pichon et al., 2014; Zattin et al., 2005). This tectonic event is the result of the Anatolian plate moving westward and all these tectonic deformations are described as an extensional tectonic regime and are revealed in the form of N–S extension and E–W compression in the Aegean region (Okay & Satir, 2000). Three models were proposed for the extension mechanism in the region. The first, proposed by Dewey and Şengör (1979), is described as a westward escape of the Anatolian plate. The collision between the Arabian platform and Anatolia compressed eastern Anatolia and transferred the stress to the west because Eurasia behaves like a craton. This stress transfer caused extension at the Aegean Sea and western Anatolia. However, the collision between the Arabian platform and Anatolia was at ~15 Ma ago and the detection of Oligocene basins in Western Anatolia invalidated this model (Okay, 2001). The second model is gravitational collapse proposed by Seyitoğlu and Scott (1996). The lithosphere was thickened up to 55 km because of the collision and tended to collapse under its own weight and induce the extension of the Aegean Sea and western Anatolia. The third model, which is the most widely accepted model today, is the extension triggered by the retreating Hellenic trench. It was suggested that the convergence velocity between Africa and Eurasia decreased, and compression in western Anatolia was diminished; this then triggered the slab retreat and started extension in the region (Jolivet & Faccenna, 2000; Jolivet & Brun, 2010; Jolivet et al., 2013a, b).

In the study area, extensively observed units are Oligocene–Middle Miocene Çan volcaniclastics in the site consisting of andesite, trachyandesite, basaltic andesite lavas, and rhyolitic tuff. Hydrothermal alteration of Çan volcanics has caused the formation of large kaolin deposits and also silica sinter precipitation in the region (Ercan et al., 1995; Ercan et al., 2022; Erenoğlu, 2017; Türkdönmez & Bozcu, 2008). Volcanic rocks were intercalated with lignite, conglomerate, sand, clay, and carbonate during the sedimentary process in the Miocene; Çan volcanics were covered by all of these volcano-sedimentary units. The kaolin deposits of Bahadırlı, Çaltıkara, and Duman all occur within the Çan volcanics in the Etili area on the NE–SW- and E–W-trending faults that constitute the Çan-Etili-Bayramiç Fault Zone (Fig. 1).

https://doi.org/10.1007/s42860-022-00214-4 Published online by Cambridge University Press

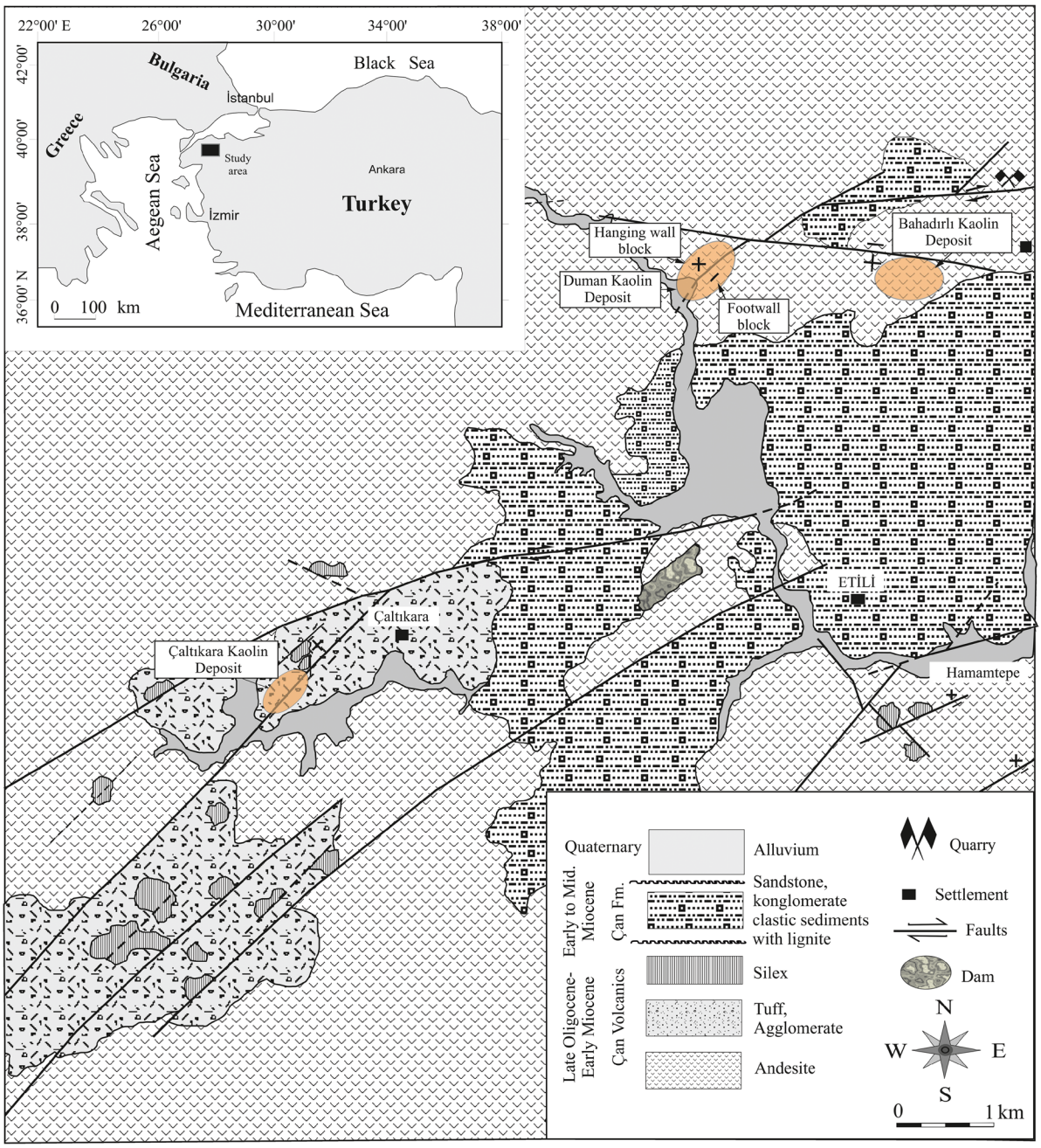

Fig. 1 Geologic map of the study area. The map in the upper left indicates the location of western Turkey and neighboring regions. The regions marked with orange indicate the approximate locations of the Duman, Bahadırlı, and Çaltıkara kaolin deposits (Ercan et al., 2022; Türkdönmez & Bozcu, 2012)

Geological and lithological properties of the kaolin deposits

As a result of field work in BKD, DKD, and CKD, argillization was determined to have occurred intensely in the tuffs. The tuffs are observed as block and ash flow type. Various colorations and different secondary mineral developments occurred with the effect of alteration in the tuff. These colorations are characteristic oscillatory zoning observed in the tuffs

https://doi.org/10.1007/s42860-022-00214-4 Published online by Cambridge University Press

of the Çan volcanics (Erenoğlu, 2017). The alteration effect is observed in all of the mineral groups in the tuffs, and is more intense in K-feldspars, plagioclase, and the matrix. On the other hand, silicification-related quartz is another typically detected mineral group.

The Bahadırlı kaolin deposit (BKD) is located within the Oligocene Çan volcanics that are east of the study area. This quarry covers ~20,000 m^2 (200 m × 100 m) and extends parallel to a fault in the E–W direction which is a branch of the Çan-Etili-Bayramiç fault zone and kaolinization occurred around this fault. The layers in different colors are quite evident at BKD (Fig. 2a, b). The red silicified rocks and less altered maroon iron oxide-rich tuff are observed at the base levels, and beige kaolinite increases at the middle levels of the deposits. Incarnadine, reddish-pink, greenish-gray colored iron oxide- and silica-rich thin bands are interstratified within kaolin-rich layers. The BKD begins with the purple firing zone at the east end and ends with the white-yellow and stockwork-textured opals in the west. The silicified tuff layer covers mostly the upper levels of the deposit. The tuffs affected by silicification are hard and compact, while the tuffs in the deposit unaffected by silicification are porous and brittle (Fig. 2a, b).

The Duman kaolin deposit (DKD), with an approximate size of 87,500 m^2 (500 m × 175 m), is located within the Çan volcanites. The DKD extends in a NE–SW direction and is located on the same Çan-Etili-Bayramiç fault. In this quarry, kaolinization occurred on two different slopes which are related to faulting, these are the hanging wall block and the footwall block. Altered beige tuffs of the Çan volcanics are found in the upper zones of the hanging wall side, and white-beige colored kaolin is located at the lower levels. The footwall side starts with white altered kaolins at the lower levels and continues with silty, sandy, coaly units of different thicknesses containing lapilli tuff and conglomeratic layers belonging to the Çan Formation. These sedimentary layers start with coal-bearing clay at the base and reach up to 50 cm thick. The overlying coal layer, up to 3 m thick, is intercalated with the upper parts of red, yellow, brown, and beige sediments and volcanics. Slump, fold, and fracture structures were formed from the effect of tectonism in the sedimentary layers (Fig. 2c, d). The upper levels of the footwall are composed of altered tuffs.

The Çaltıkara Kaolin Deposits (CKD), located in the Çan Volcanics to the south of the study area, cover ~35,000 m^2 (200 m × 175 m). The deposit extends NE–SW and is a fault-controlled deposit. This fault, which is a branch of the NE–SW trending Çan-Etili fault, is a right-lateral strike-slip normal fault, and kaolinization developed in parallel with this fault. White and beige massive kaolinization is common in the quarry, and an epithermal vein intrusion rich in ore minerals, including pyrite, galena, and bornite, is found in the upper levels of the quarry. In addition, reddish and purplish iron oxide minerals are observed in a wide area developed along the fault zone (Fig. 2e).

Methods of Study

Geological maps at 1/25,000 were made, based on detailed geological observations and representative sampling at open quarries for analysis. The petrological properties of samples collected from kaolins and basement rocks were determined in thin section using a Leica DM4500P polarizing microscope at the Istanbul Technical University (ITU) in İstanbul (Turkey). X-ray diffractometry (XRD) analyses were performed on 15 samples from BKD, 31 samples from DKD, and 12 samples from CKD; this was used to determine the mineralogical compositions. Analysis was carried out using a Bruker D8 Advance model instrument with CuKα radiation and using a LynxEye detector at Istanbul Technical University (ITU) in İstanbul, Turkey. XRD data were collected using CuKα radiation (40 mA, 40 kV), scanning range of 2–72º2θ, and step-size of 0.01940º for bulk random mounts, and 2–42º2θ, and step size of 0.005º2θ for oriented mounts, 0.1 s/step, 0.2 mm divergence slit, Ni filter, and a LynxEye1 solid-state detector. The micro-morphological properties of the kaolins and other minerals were detected using a ZEISS GeminiSEM 500 model Field Emission Scanning Electron Microscopes (FE-SEM) at 15 kV accelerating voltage, 5–15 mA current, and 10–20 s counting time for each element Science and Technology Research and Application Center (BİTAM) at the Necmettin Erbakan University in Konya, Turkey. An

https://doi.org/10.1007/s42860-022-00214-4 Published online by Cambridge University Press

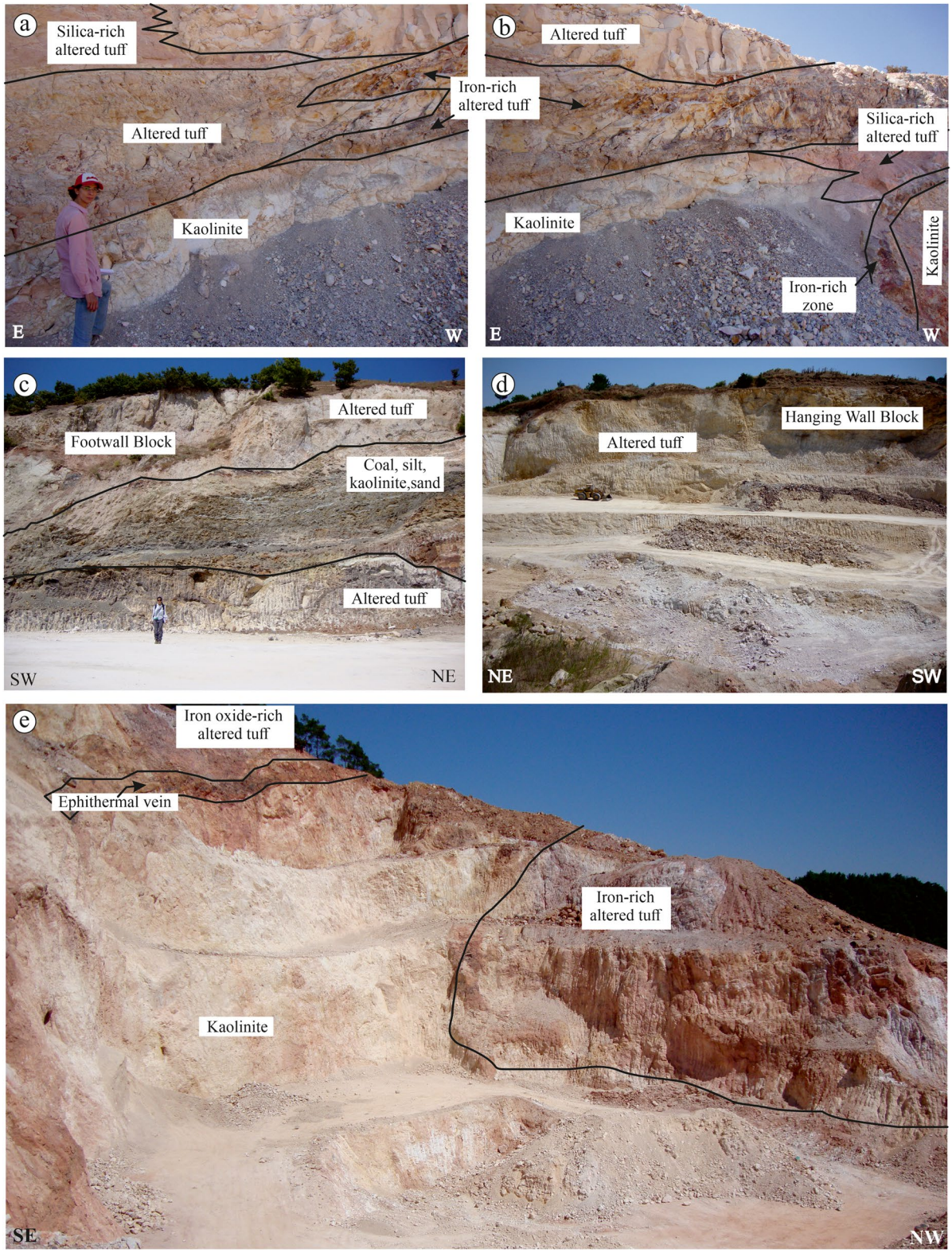

https://doi.org/10.1007/s42860-022-00214-4 Published online by Cambridge University Press

◂**Fig. 2** Photographs of the kaolin deposits of the study area: **a** SW-NE side of the DKD containing coal, silt, and clay layers between the altered tuffs layers, **b** NE-SW side of the DKD containing clay and altered tuffs, **c**,**d** siliceous and iron-rich altered tuff, altered tuffs, and kaolinite layers of the BKD images, **e** image of CKD containing epithermal vein and iron-rich kaolin and altered tuffs

SPI-MODULE® sputter coater was used for Au coating under operating conditions of 2 mbar, 15 mA, and 50 s. This provides a coating which is ~150 Å thick.

Major and trace element analyses were performed using Spectro Ciros Vision inductively coupled plasma-optical emission spectrometry (ICP-OES) for Ba, Sc, Mo, Cu, Pb, Zn, Ni, and As at the ACME Laboratory, Vancouver, Canada. The detection limits for major elements, trace elements, and rare-earth elements (REE) were 0.01 to 0.1 wt.%, 0.1 to 5 ppm, and 0.01 to 0.5 ppm, respectively. Some trace and REE analyses were performed using a PerkinElmer Elan 6100 ICP-MS instrument at the ITU-Geochemistry Research Laboratory (JAL) in İstanbul, Turkey. The detection limits for REE analyses were 0.01 ppm. $\delta^{34}S$ isotopic analyses were performed on three samples from the BKD, on seven samples from DKD, and on six samples from the CKD, for which purities of alunite were determined by XRD. In addition, one galena and one pyrite sample were taken from the copper mine for $\delta^{34}S$ isotopic analysis and the isotopic contents were analyzed; SO_2 produced by heating alunite at 1050°C was analyzed using a Finnigan MAT 252 gas-source mass spectrometer at the University of Georgia (UGA) in Georgia, USA. Canyon Diablo Troilite (CDT) was used as the standard and the accuracy is ~ ± 0.2‰. Separation of kaolins (<2 μm) for isotope analysis: firstly, the kaolin-rich samples were milled for XRD analysis to reduce the particle size to <10–20 mm, and samples were dispersed in distilled water by ultrasonic vibration. Then, the classification of size fractionation of the clays (<2 mm) was performed using a centrifuge, and clay paste homogenized on the smear glass. Finally, oriented clay bases were prepared by air drying the glass slides (Moore & Reynolds, 1989). The purity of kaolin samples was determined by XRD; $\delta^{18}O$ and δD isotopic analysis were performed on three kaolin samples from BKD, on ten from DKD, and on three from CKD. The $\delta^{18}O$ and δD values of kaolinite were determined using the Finnigan MAT 252 or Finnigan Delta E spectrometers at the same university in Georgia, USA. The best available three alunite samples were identified using XRD analysis and $^{40}Ar/^{39}Ar$ radiometric age analysis was performed by incremental heating at the University of Michigan, Michigan, USA. The incremental heating method utilizes a double vacuum resistance furnace similar to the design of Staudacher et al. (1978). These analytical methods and data-treatment procedures are included in detail in the studies by Justet and Spell (2001) and Spell and McDougall (2003).

Results

Mineralogical and Petrographic Studies

In the present study, mineralogical and petrographic investigations were performed to reveal the compositions and textural properties of the Oligo-Miocene lavas of the Çan volcanics, where the intense alteration occurred. These volcanic units are mostly of andesite, basaltic-andesite, and basaltic-trachyandesite types (Türkdönmez & Bozcu, 2008). Plagioclase, K-feldspar, amphibole, biotite, and rarely clinopyroxene crystals with different ratios were detected in these rocks (Fig. 3). The tuffs are observed as block- and ash-flow type and kaolinization is most evident in the tuffs. K-feldspar, plagioclase, and the matrix have been mostly kaolinized while biotite and amphiboles were Fe-oxidized as seen in the photomicrographs (Fig. 3).

X-ray diffraction of the BKD samples detected kaolin, quartz, smectite, alunite, and lesser amounts of plagioclase and K-feldspar (Fig. 4a and Table 1). The mineral association representing the lower levels of BKD is kaolinite + quartz ± alunite ± plagioclase ± K-feldspar (Table 1; BH-1 to BH-9-d). However, at middle levels, the quartz content decreases, while smectite increases (Table 1; BH-10-A to BH-10-F). While the kaolin and alunite contents decrease, the amount of quartz increases in the upper levels (Table 1; BH-11 to BH-15-u). Two types of kaolinite were observed during the FE-SEM studies of the kaolinite-rich levels: (1) equidimensional, euhedral with < 6–7 μm kaolinite, and (2) small-grained, anhedral with dimensions of 1–3 μm. The first type is an equidimensional oriented kaolinite form which occurs in partially vermiform booklet stacks (Fig. 5a, b). The second type is randomly

https://doi.org/10.1007/s42860-022-00214-4 Published online by Cambridge University Press

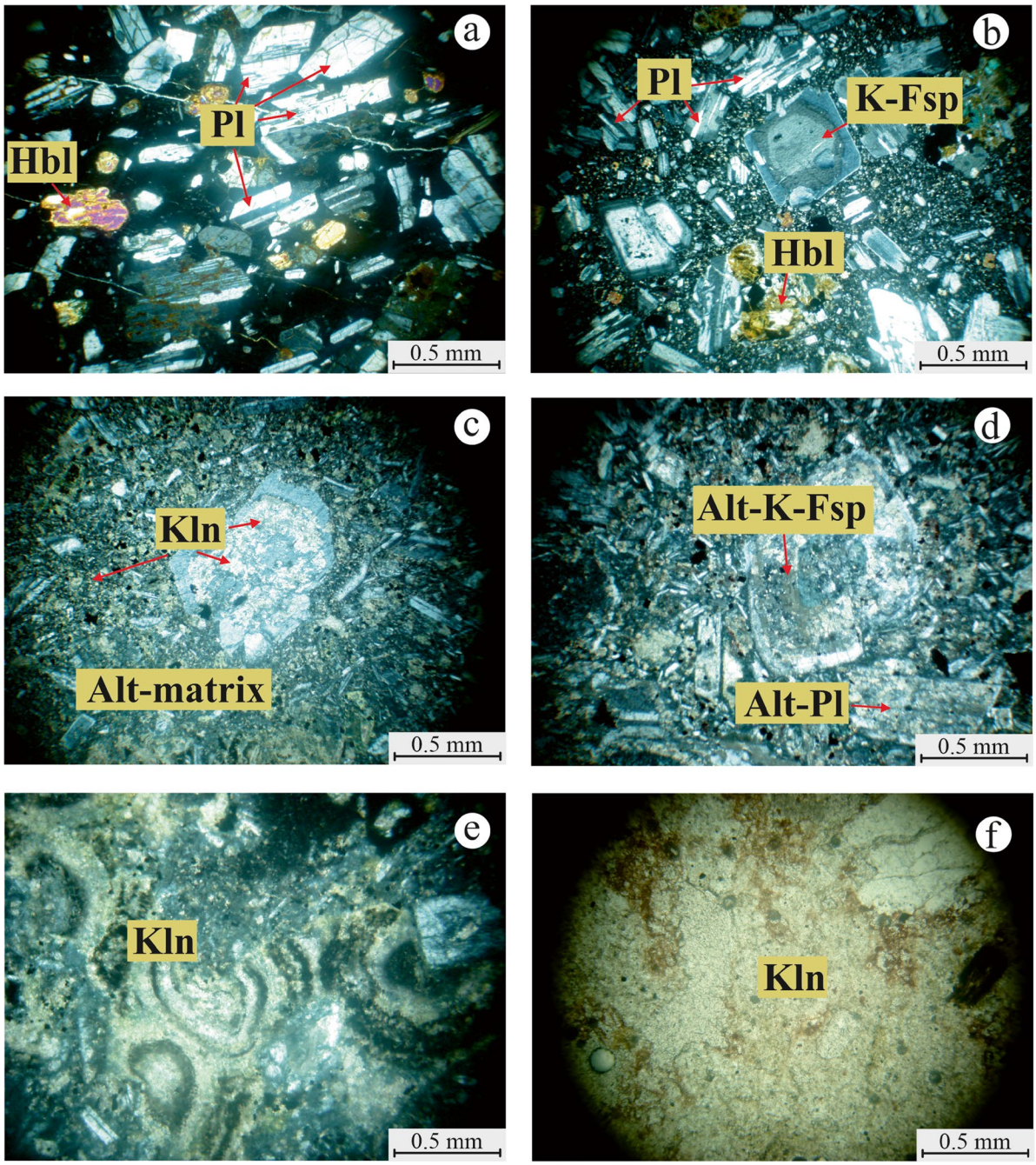

Fig. 3 Optical microscopy images of Çan volcanics: **a** optical photomicrograph (crossed-polarized light) showing twin planes of plagioclase and slightly devitrified (altered) hornblende within the volcanic glass of the andesite; **b** slightly altered K-feldspars and plagioclases, Fe-oxidized hornblende within the volcanic glass of the andesite; **c**,**d** kaolinized plagioclase and K-feldspar phenocryst within the altered volcanic groundmass of the trachyte, the opaque crystals may be pyrite that have been subjected to partial oxidation; **e**,**f** kaolinized minerals which have lost their optical properties due to alteration within the tuff (**f** – plane-polarized light). The light gray patches are K-feldspar and plagioclase (note the local presence of zonation of the Fe-oxide pigment in the photomicrograph)

https://doi.org/10.1007/s42860-022-00214-4 Published online by Cambridge University Press

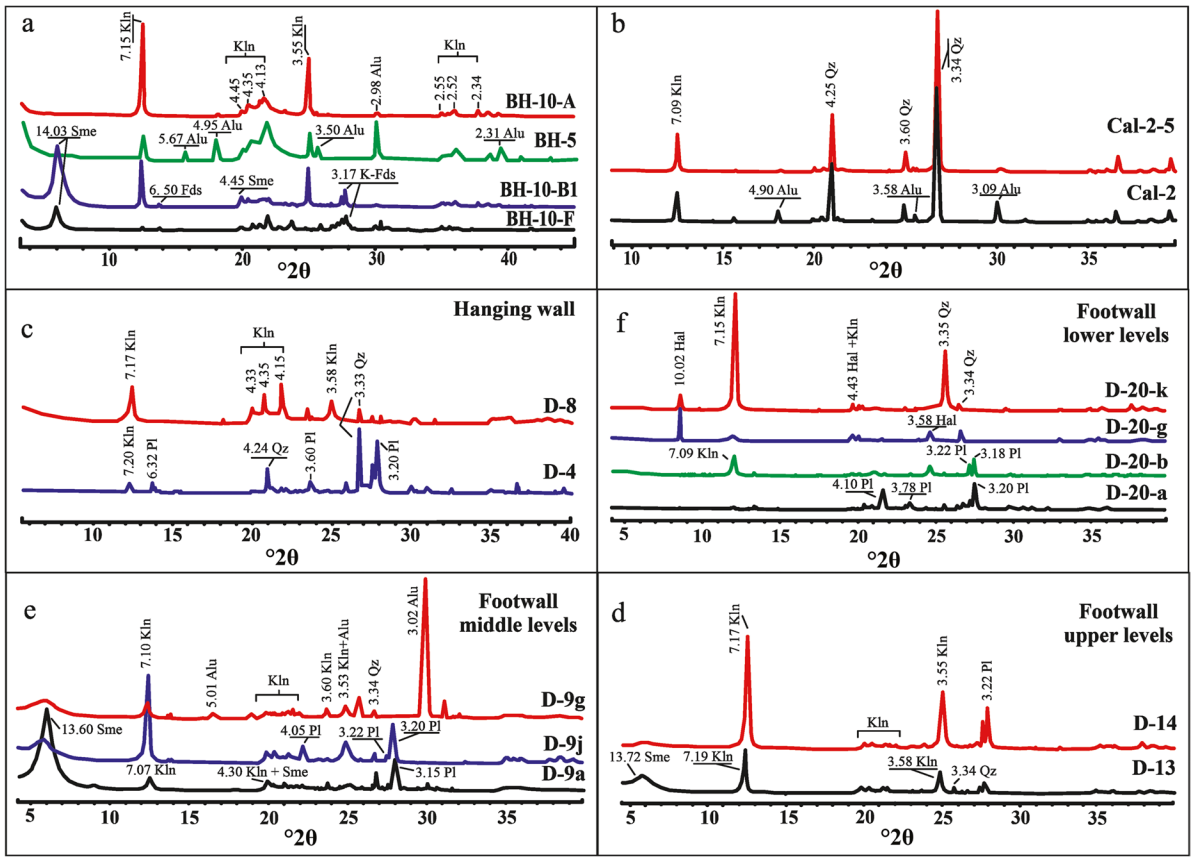

Fig. 4 XRD patterns of the kaolin deposits: **a** BKD, **b** CKD, **c** hanging wall of the DKD, **d** lower levels of the DKD, **e** middle levels of the DKD, **f** upper levels of the DKD. Kln: kaolinite; Alu: alunite; Qz: quartz; Sme: smectite, Pl: plagioclase, Hal: halloysite, K-Fs: K-feldpar (abbreviations from Whitney & Evans, 2010)

oriented crystal platelets (Fig. 3c). Well formed cubic-like alunite crystals which varied from 5 to 10 μm in size were observed. Dissolution pitting was detected in some of the alunite crystals (Fig. 5d). Halloysite has a tubular morphology with outer diameters of 1–2 μm (Fig. 5c, d).

In the XRD analysis of CKD samples, kaolin and quartz minerals were detected in all samples and this mineral couple was accompanied by small amounts of alunite. The amount of quartz increases nearer to the fault zone (Fig. 5b and Table 1). A commonly observed (by SEM) clay mineral, equidimensional and randomly oriented, is accompanied mostly by euhedral and anhedral quartz grains. Well crystallized <1–3 μm kaolinite plates look as though they have been sprinkled on the quartz (Fig. 5e, f). Spherical and euhedral quartz coexists, the latter crystals range up to 30 μm in diameter; the spherical quartz ranges between <1 and 30 μm (Fig. 5g, h). Microcrystalline anhedral iron-oxide minerals (<1 μm) were often randomly coated on the surface of the clay minerals and other quartz crystals (Fig. 5h).

Kaolin is the most frequently detected alteration mineral in XRD analysis of DKD samples. In hanging wall block samples, a mineral association of kaolinite + quartz ± alunite ± plagioclase ± K-feldspar ± smectite was detected (Fig. 4c and Table 1). Three different mineral associations were determined by XRD analysis of samples from the footwall block: (1) a kaolinite ± quartz ± plagioclase ± K-feldspar ± smectite association for samples from the lower levels of the footwall block (Fig. 4d); (2) a kaolinite + smectite ± quartz ± plagioclase ± alunite association from the middle levels of the footwall block (Fig. 4e); and (3) a kaolinite + plagioclase + smectite ± quartz ± K-feldspar ± gypsum association for

https://doi.org/10.1007/s42860-022-00214-4 Published online by Cambridge University Press

Table 1 Mineralogical contents of samples from the Bahadırlı, Çaltıkara, and Duman kaolin deposits

Sample ID.		Kaolin	Quartz	Alunite	Smectite	Plagioclase	K-feldspar	Carbonate	Gypsum	Mica
Bahadırlı Kaolin Deposit										
BH-1		****	acc	acc		acc				
BH-5		**	acc	**						
BH-6		****	acc			*				
BH-9-a		***	*							
BH-9-d		***	**	*	acc					
BH-10-A		****	acc	acc						
BH-10-B1		**		acc	**		*			
BH-10-B2		***			**					
BH-10-C		***		*						
BH-10-D		****		acc						
BH-10-F		acc		acc	***		**			
BH-11		*			***		*			
BH-12		**	***			*				
BH-15-a			***		**					
BH-15-u		*			**	*	*			
Çaltıkara Kaolin Deposit										
Çal 2		*	**	*						
Çal 2.2		acc	****	acc						
Çal 2.4		*	**	**						
Çal 2.5		**	**	acc						
Çal 7		**	***							
Çal 9		*	****							
Çal 10		***	**							
Çal 11		****	*	acc						
Çal 12		***	*	acc						
Çal 13		***	**							
Çal 14		acc	****	acc						
Çal 15		*	****	acc						
Duman Kaolin Deposits										
D1	Hanging Wall Samples	**	**			acc		acc	acc	
D2		**	***							
D3		***	**		acc					
D4		**	*			**		*	*	
D5		**	**		acc					
D6		***	**			*		acc	acc	
D7		***	**							
D8		***	*	*		acc		acc		

https://doi.org/10.1007/s42860-022-00214-4 Published online by Cambridge University Press

Table 1 (continued)

Sample ID.		Kaolin	Quartz	Alunite	Smectite	Plagioclase	K-feldspar	Carbonate	Gypsum	Mica
D-9a	Foot Wall Sediment Rich-levels(Middle Levels)	*	acc	acc	****	*				
D-9b		*			**	**		**		
D-9c		**	*		**	acc		acc		
D-9d		*	acc		*	**		**		
D-9e		*			***	*		*		
D-9f		*			***	*		*		
D-9g		*	acc	****	*					
D-9j		***	acc		*	*		*		
D10	Foot WallUpper Levels	**	*		*	*		*		
D11		**	*		**					*
D12		*	*		**	*		*		
D13		***	acc	*	*	*		*		
D14		***		*	acc	*		*		
D15		*			**	*		*		*
D16		acc			*	*		*		***
D-20-a	Foot WallLower Levels	acc				****	acc	****	acc	
D-20-b		**	*			**	*	**	*	
D-20-c		****					*		*	
D-20-d		***			*		*		*	
D-20-e		***			*		*		*	
D-20-k		***	*							
D-20-f		****			*					
D-20-g		****				*		*		

samples from the upper levels of the footwall block (Fig. 4f and Table 1). FE-SEM images of kaolins from the section representing the hanging wall block showed them to be generally equidimensional and book-like but the edges and corners of the kaolin crystals were ragged (Fig. 6a, b). Book-like kaolinites were commonly observed among the altered surface of the coarse and euhedral feldspar minerals. In addition, weathering of halloysite and kaolinite minerals from feldspar minerals was typified quite well in FE-SEM images. Kaolinite to halloysite transformation was observed in the form of bending of kaolinite plates from the edges (Fig. 6c, d). Halloysite was more abundant in the FE-SEM images of samples from the footwall block of the quarry. Halloysite appeared with a hollow open-ended tubular morphology, having internal lumen diameters of 50–80 nm and outer diameters of 100–180 nm which were oriented randomly with varying lengths and thicknesses (Fig. 6e, f). Micro-morphological FE-SEM characterization of DKD samples revealed the 'halloysitization' of feldspars (Fig. 6). In addition, from FE-SEM studies, fossil remnants of the microbiota structures which developed intergrowths with clays on the altered mineral surfaces were detected in the altered samples of the hanging wall of the DKD. The structures of these microorganisms are rotiform and each branch was up to <0.5 μm thick (supplementary material Table S1 ESM_1PDF).

Geochemistry of the Kaolin Deposits

Chemical analyses of 12 samples from two different rock types was performed: (1) 11 clay-rich samples from the alteration zone; and (2) one tuff sample, representing the host rocks. Major oxide concentrations of the two altered samples from BKD were: Al_2O_3 10.78–26.23 wt.%, SiO_2 54.08–74.90 wt.%, Fe_2O_3

https://doi.org/10.1007/s42860-022-00214-4 Published online by Cambridge University Press

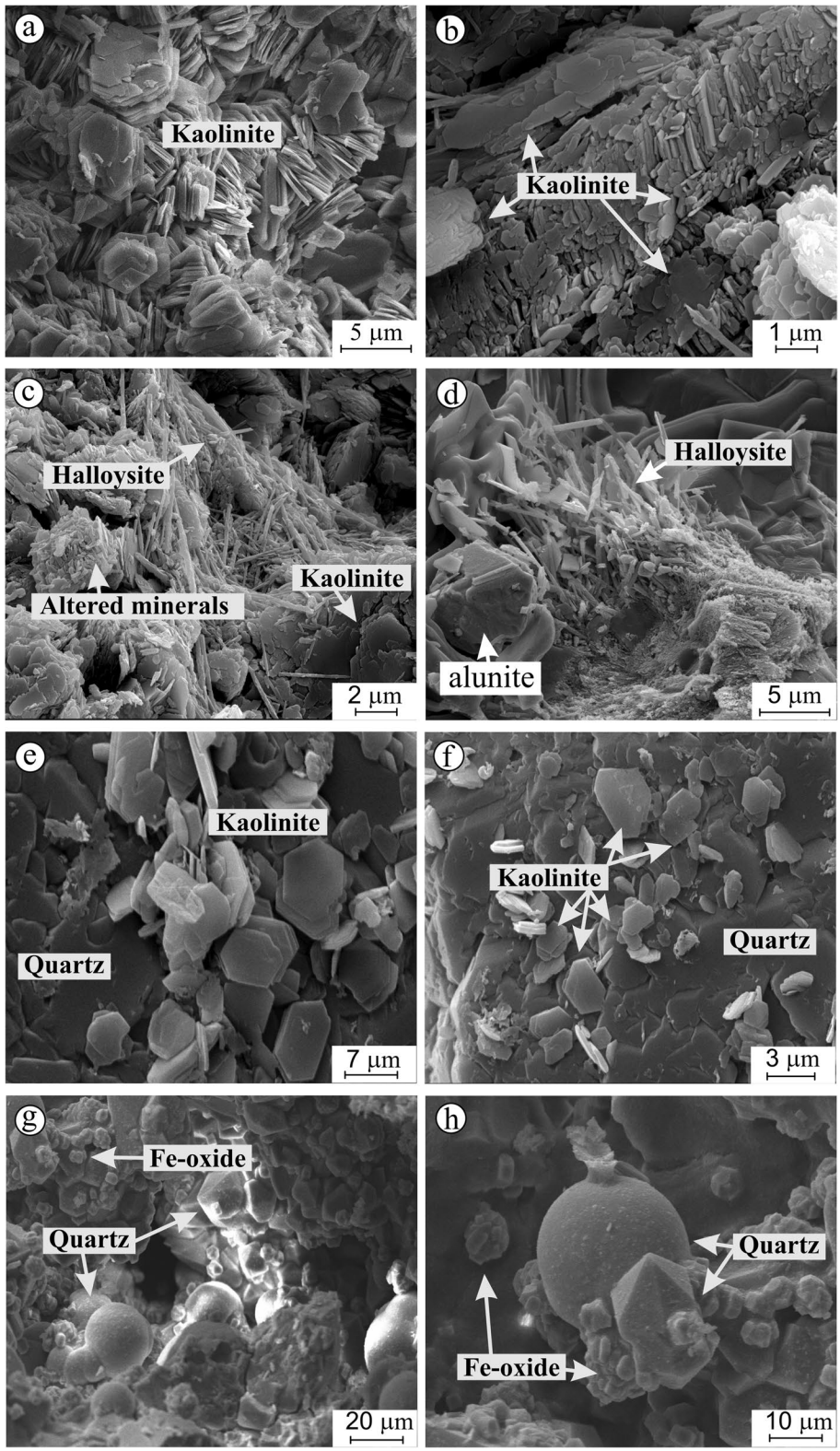

https://doi.org/10.1007/s42860-022-00214-4 Published online by Cambridge University Press

◂**Fig. 5** FE-SEM images of minerals from the BKD and CKD: **a** equidimensional and book-shaped kaolinite crystals; **b** vermiform and randomly oriented kaolinite crystals, BKD; **c** randomly scattered kaolinite and halloysite minerals, BKD; **d** well-formed cubic-like alunite crystals and halloysite tubes observed mostly at the surface, BKD; **e**,**f** randomly scattered kaolinite on the quartz, BKD; **g**,**h** spherical and euhedral quartz with iron-oxide minerals, CKD

nearly 0.20 wt.% for the two samples; the Na_2O, Ca_2O, and K_2O contents were small (Table 2). The maximum and minimum major oxide contents of the four samples of the CKD are 12.93–19.38 wt.% for Al_2O_3, 52.31–66.13 wt.% for SiO_2, 0.28–6.79 wt.% for Fe_2O_3, 0.03–7.28 wt.% for Ca_2O, 0.26–4.34 wt.% for Na_2O, and 1.96–4.03 wt.% for K_2O. In the CKD samples, the Fe_2O_3 contents of the samples taken from nearer the fault was large (M-26, M-27). Moreover, the CaO and Na_2O contents of these samples are also large. The major oxide contents of five DKD samples ranged as follows: Al_2O_3 from 17.6 to 32.85 wt.%, SiO_2 from 40.66 to 68.22 wt.%, Fe_2O_3 from 0.94 to 8.56 wt.%; the Na_2O and Ca_2O contents are small but the K_2O contents ranged from 0.31 to 5.78 wt.% (Table 2).

The Ba contents of the BKD, CKD, and DKD samples are close and range as follows: 833–1430, 608–1071, and 742–1503 ppm, respectively. The Ba content of the host rock was 921 ppm. The Sr concentrations of the BKD, CKD, and DKD samples range 737.5–834.5, 567.7–1459.6, and 50.7–93.4 ppm, respectively. The Sr content of the DKD samples is small compared to other deposits and host rocks (205.6 ppm) (Table 2). The Rb concentration in some samples of DKD was much greater (13.2–184.3 ppm) than those of the BKD and CKD deposits and host rock (Table 2). The Y, La, and Ce contents of the BKD samples ranged: 14.4–14.7, 17.6–33.3, and 33.2–59.6 ppm, respectively. The Y, La, and Ce concentrations of the CKD samples ranged: 1.4–35.7, 7.8–33.6, and 9.6–64.5 ppm, respectively. The Y, La, and Ce contents of the DKD were greater than the other deposits, ranging from 20.9 to 32.85, 40.1 to 61.2, and 79.0 to 190.9 ppm, respectively. The Y, La, and Ce contents of the host rock were small at 19.3, 0.6 and 0.5 ppm, respectively (Table 2). As can be seen from Table 2, the REE contents of the DKD are generally greater than the other two deposits and host rock.

Stable Isotope Geochemistry of the Kaolin Deposits

$\delta^{34}S$ isotope analysis was performed on alunite minerals, the purity of which was determined by XRD analysis. The $\delta^{34}S$ values of the BKD samples were enriched at 19.8 and 20.2‰ and the samples were slightly depleted at –6.3‰. The $\delta^{34}S$ isotopic DKD alunite values were slightly depleted at –0.9 and –1.7‰ (DD-1 and DD-2) whereas the DC-1, DC-2, DC-3, and DC-4 samples $\delta^{34}S$ isotopic contents were heavily depleted at –15.3 to –17.2‰. The DU-1 sample $\delta^{34}S$ isotopic content was highly enriched at 10.5‰. Three $\delta^{34}S$ isotopic values of the CKD samples ranged from 5.7 to 16.8‰; these samples were enriched in $\delta^{34}S$. The $\delta^{34}S$ isotopic contents of galena and pyrite were slightly depleted at –0.3 and –0.1‰, respectively (Table 3).

$\delta^{18}O$ and δD analyses were performed on the purified and enriched kaolin samples. The $\delta^{18}O$ values of the BKD kaolin samples ranged from 11.8 to 17.0‰ and δD values ranged from –99 to –93‰. The $\delta^{18}O$ values of the DKD kaolin samples ranged from 18.3 to 10.3‰ and δD values ranged from –70 to –102‰. The $\delta^{18}O$ ranged from 10.3 to 12.2‰ and δD from –49 to –82‰ for the CKD (Table 3).

Geochronology

Three pure alunite samples taken from the Bahadırlı and Duman kaolinite deposits were analysed for $^{40}Ar/^{39}Ar$ age dating (Table 3). Two age dates for CKD were taken from Ercan et al. (2022). The timing of hydrothermal alteration of the kaolin deposits was Oligocene-based on the data obtained from $^{40}Ar/^{39}Ar$ dating: (1) 32.2 ± 1.0 to 32.4 ± 1.2 Ma in the BKD; (2) 29.7 ± 0.1 Ma in the DKD; and (3) 22.6 ± 0.2 to 28.4 ± 0.4 Ma in the CKD.

Discussion

Mineralogical Characterization of Quarries

Detailed assessment of kaolin and alunite group minerals in the alteration zones of the Bahadırlı, Duman, and Çaltıkara kaolin deposits provided more detailed information on acid sulfate-rich geothermal fluids. Photomicrograph investigations indicated that secondary kaolinization occurred from primary

https://doi.org/10.1007/s42860-022-00214-4 Published online by Cambridge University Press

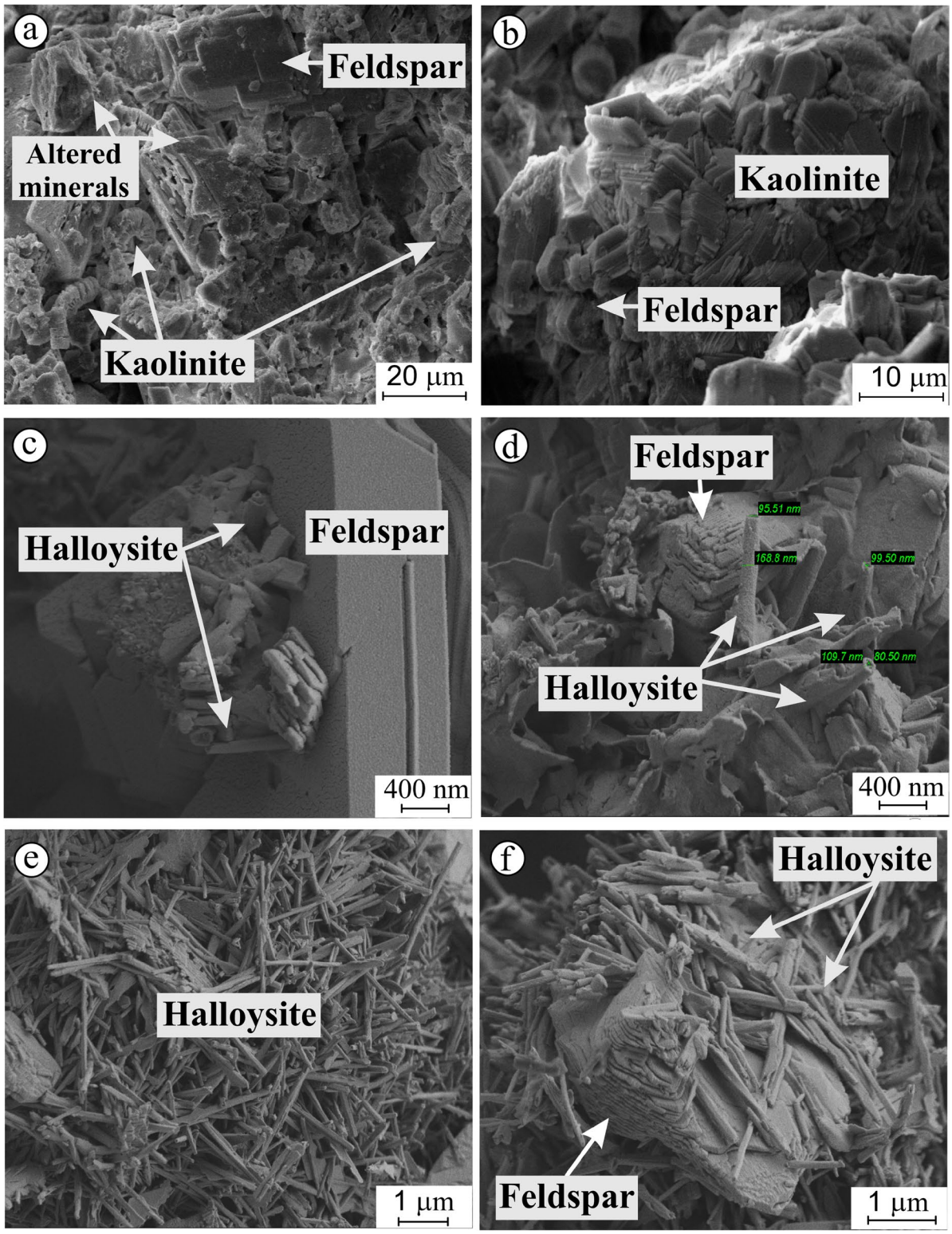

https://doi.org/10.1007/s42860-022-00214-4 Published online by Cambridge University Press

◂**Fig. 6** FE-SEM images of altered minerals from the DKD: **a** vermiform (book-shaped) kaolinite crystals with euhedral altered feldspar minerals; **b** kaolinized feldspar minerals; **c** transformed halloysite mineral from feldspar minerals; **d** alteration of halloysite and kaolinite from feldspar and the bending of the kaolinite; **e** open-ended tubular halloysite crystals; **f** advanced altered feldspar with associated halloysite randomly scattered on the feldspar

K-feldspar, plagioclase phenocrysts, and the matrix of the porphyritic textured lavas and tuffs (Fig. 3).

The mineralogical association of BKD was kaolinite + quartz ± alunite ± smectite ± plagioclase ± K-feldspar (Fig. 4a). The increasing alunite content and the small smectite content in the lower zones where kaolinization is significant indicated formation in a low-pH environment; the increasing amount of smectite in the samples taken from the upper zones was relatable to the increase in pH, however. A kaolinite + quartz + smectite mineral assemblage in the upper zone represented the areas in which the hydrothermal solution pH is neutralized vertically. This may be interpreted as meteoric water inflow. The mineralogical composition of CKD is quite homogeneous and consists of kaolinite + quartz ± alunite (Fig. 4b), which is the most typical mineral association of hydrothermal alteration zones indicating an acidic environment (Hedenquist et al., 2000). The mineralogical composition of the DKD hanging wall block samples was similar to that of the BKD, but the footwall block exhibited a different and heterogeneous mineralogical distribution. The hanging wall block was raised by tectonic activity; the Miocene lacustrine sediments above this wall were probably eroded completely and the consequent hanging wall block represents the Oligocene. Miocene lacustrine deposits in the footwall block were not affected by erosion; the mineralogical association of this block is more complex than that of the hanging wall block, therefore. Footwall blocks were considered as lower levels, middle levels, and upper levels in terms of mineralogical variations. The mineralogical composition of the lower levels of the footwall block is similar to that of the hanging wall block; during the deposition of Miocene lacustrine deposits, the middle and upper levels were affected by freshwater flow into the lake environment and the solution acidity decreased, therefore. In conjunction with increasing pH, smectite became the dominant mineral. Primary plagioclase minerals were also observed with the decrease in solution acidity at these levels. The gypsum minerals detected in some samples of the upper levels of the footwall block were associated with lacustrine deposits rather than hydrothermal alteration because gypsum was not detected in any of the other hydrothermal kaolin deposits in the region.

Kaolinization is well developed in the kaolinite-rich zone of the BKD, and semi-booklet and randomly scattered kaolinite crystals were detected in the FE-SEM images (Fig. 5). Kaolinite crystal dimensions vary generally between 2 and 5 μm. Randomly scattered kaolinite has similar dimensions to the book-shaped kaolinite. Book-shaped and vermiform kaolinites were observed with the altered feldspar minerals in the hanging wall samples of the DKD (Fig. 6). When the increase in crystallization index in kaolinization occurred, it proceeded by gradual structural changes concomitant with crystal coarsening and changes from booklet to blocky (vermiform) morphology (Beaufort et al., 1998). This morphological progress indicates that the advanced stage of kaolinization is usually possible with increasing temperature and decreasing pH. Randomly oriented kaolinite crystals were observed commonly in the FE-SEM images of the CKD and this crystal structure is usually formed in alteration zones where low temperatures were effective (Bailey, 1993).

In XRD analysis of the BKD, CKD, and DKD, alunite was detected in all deposits, but only in FE-SEM analyses of BDK samples were alunite crystals of <10 μm observed (Fig. 5d). Alunite found typically in low-temperature and steam-heated environments have grain sizes of 20–50 μm, whereas grain sizes of hypogene alunite are coarse and in the range of 50 to 100 μm (Hedenquist et al., 2000). This suggests that alunite in the BKD formed at relatively low temperatures in a steam-heated environment. Dissolution pits were observed on alunite crystal surfaces and they were interpreted to be the result of either secondary surface weathering or of dissolution under highly acidic conditions (Ercan et al., 2016). In Fig. 5d, alunite intergrowth with halloysite was observed, and one or two halloysite tubes were noted on the alunite crystals. The mineral association of halloysite and alunite was interpreted as representing an acidic (< 4 pH) environment of formation (Ece et al., 2008). Halloysite tubes were observed in some samples from BKD and in footwall block samples from DKD (Fig. 5c, d and 6e, f). The

https://doi.org/10.1007/s42860-022-00214-4 Published online by Cambridge University Press

Table 2 Chemical analyses of the BKD, CKD, DKD, and parent rocks (major elements in wt.%, trace and rare earth elements in ppm). B represents BKD samples, M represents CKD samples, and D represents DKD samples. T represents the tuff taken from the region and least affected by alteration

	BKD		CKD				DKD					Host-rock
	BH-9d	BH-1	M-26	M-27	M-3	M-28	D1	D2	D6	D8	D9 J	T
%												
SiO_2	74.90	54.08	55.26	55.1	52.31	66.13	59.01	63	40.66	68.22	47.6	68.97
Al_2O_3	10.78	26.23	17.03	17.21	19.38	12.93	17.6	19.7	32.85	17.54	23.25	14.18
Fe_2O_3	0.2	0.19	6.71	6.79	0.28	0.51	4.73	2.73	6.95	0.94	8.56	1.54
MgO	0.02	0.01	1.95	1.67	<0.01	<0.01	0.09	0.06	0.13	0.15	0.56	0.37
CaO	0.19	0.07	5.84	7.28	0.04	0.03	0.31	0.27	0.36	0.39	1.35	1.63
Na_2O	0.11	0.09	4.34	3.78	0.26	0.38	1.02	1.9	0.04	2.3	0.54	3.54
K_2O	1.3	1.45	2.35	1.96	4.03	2.58	5.78	5.65	0.31	5.48	1.67	4.21
TiO_2	0.21	0.37	0.9	0.92	0.49	0.69	0.37	0.31	0.84	0.33	0.76	0.27
P_2O^5	0.21	0.17	0.39	0.42	0.3	0.17	0.03	0.04	0.17	0.03	0.08	0.08
MnO	<0.01	<0.01	0.16	0.17	<0.01	<0.01	<0.01	<0.01	0.18	<0.01	0.02	0.14
Cr_2O_3	<0.002	<0.002	0.002	<0.002	0.005	0.004	<0.002	<0.002	<0.001	<0.002	<0.002	0
LOI	11.7	16.9	4.8	4.4	22.5	16.2	10.5	6.07	17.01	4.3	15.07	4.3
Sum	99.68	99.59	99.7	99.73	99.56	99.62	99.44	99.73	99.32	99.68	99.44	99.09
TOT/C	0.03	0.04	1.07	0.8	0.03	0.22	–	–	–	<0.02	–	–
TOT/S	1.95	2.21	<0.02	<0.02	6	4.6	–	–	–	<0.02	–	–
ppm												
Ni	<20	<20	<20	<20	<20	<20	<20	<20	<20	<20	<21	13
Sc	3	8	11	11	6	4				5		3
Ba	833	1430	684	608	1071	909	1503	756	834	1139	742	921
Be	4	<1	<1	4	<1	<1	–	–	–	5	–	
Co	1	2.1	20.8	16.9	3.8	13	–	–	–	1	–	26
Cs	24.4	9	1.9	2.5	<0.1	<0.1	1.09	0.95	4.73	5.27	13.27	4
Ga	16.2	22.5	18.3	19	57.3	9.4	25.51	23.09	15.30	14.03	23.42	13.2
Hf	6.9	13.2	4.8	5.6	2.2	4.1	–	–	–	7	–	4.5
Nb	12.2	22	7.7	8.2	5.6	5.7	–	–	–	17.1	–	11.3
Rb	10.3	4.3	59.6	48.7	4.9	3	14.66	13.18	165.52	184.33	37.18	137
Sn	1	3	<1	<1	1	<1	–	–	–	<1	–	–
Sr	836.5	737.5	599.4	567.7	1710.6	1459.6	50.7	77.3	69.7	93.4	67.4	205.6
Ta	0.9	1.5	0.8	0.6	0.3	0.2	–	–	–	1.2	–	–
Th	19.5	28.9	9.1	9.5	9.6	3.3	56.50	50.47	37.00	34.55	62.33	20.5
U	7.2	22.8	2.5	2.8	1.4	1.2	23.50	13.77	7.20	9.46	4.04	–
V	34	37	103	105	204	76	–	–	–	24	–	16
W	21.8	32.7	89.6	42.4	43.2	111.6	–	–	–	16.4	–	196.5
Zr	251.8	452.6	188.6	187.1	105.2	130.3	175	222	324	255.2	272	205.1
Y	14.4	14.7	35.7	34.4	1.4	2.2	27.21	21.29	32.85	30.24	20.99	19.3
La	17.9	33.3	33.6	30.2	22.1	7.8	50.94	40.09	61.15	53.74	54.00	0.6
Ce	33.2	59.6	64.5	62	38.5	9.6	190.90	81.61	79.00	102.23	97.89	0.5
Pr	3.71	6.5	8.04	7.97	3.17	1.17	9.79	8.81	13.98	10.86	10.75	0.02
Nd	15	19.8	34.4	37.2	8.1	5.3	33.70	30.12	46.52	36.51	36.23	0.8
Sm	4.43	4.35	7.26	6.89	1.03	0.33	6.18	4.80	9.32	6.46	6.54	<0.1
Eu	0.66	0.42	1.88	1.69	0.23	0.1	1.22	1.06	2.04	1.24	1.58	<0.1
Gd	4.18	3.84	6.68	6.34	0.71	0.39	5.02	4.07	7.48	5.43	6.00	0.06

https://doi.org/10.1007/s42860-022-00214-4 Published online by Cambridge University Press

Table 2 (continued)

	BKD		CKD				DKD					Host-rock
	BH-9d	BH-1	M-26	M-27	M-3	M-28	D1	D2	D6	D8	D9 J	T
Tb	0.65	0.64	1.09	1.05	0.06	0.03	0.88	0.69	1.15	0.87	0.85	< 0.1
Dy	3.41	3.87	6.36	5.65	0.23	0.41	5.14	3.64	6.06	5.03	4.78	0.09
Ho	0.62	0.5	1.25	1.33	0.06	0.04	1.03	0.68	1.08	0.99	0.82	< 0.1
Er	1.43	2.2	3.46	3.78	0.25	0.37	3.19	2.47	3.93	3.21	2.49	0.14
Tm	0.34	0.26	0.52	0.76	0.03	0.02	0.46	0.36	0.51	0.49	0.25	< 0.1
Yb	1.63	1.9	3.4	3.68	0.47	0.61	4.37	3.34	4.05	3.56	2.17	< 0.1
Lu	0.35	0.31	0.65	0.57	0.04	0.4	0.60	0.47	0.62	0.60	0.29	0.05
Mo	0.5	0.3	1	1	2.1	1	–	–	–	0.3	–	0.3
Cu	2.4	6.7	17.2	14.5	1.5	8.8	–	–	–	1.8	–	3.4
Pb	31.2	37.3	5.9	11	23.5	10.1	–	–	–	6.1	–	0.8
Zn	6	3	90	98	3	6	–	–	–	11	–	15
Ni	0.2	0.4	1.3	0.9	0.5	1.1	–	–	–	0.2	–	0.8
As	35.2	44.8	0.9	3.2	14.1	29.6	–	–	–	6.8	–	< 0.1
Cd	< 0.1	< 0.1	0.1	< 0.1	< 0.1	< 0.1	2.93	1.74	1.46	3.19	4.24	–
Sb	1.2	0.1	< 0.1	< 0.1	0.4	< 0.1	–	–	–	< 0.1	–	–
Bi	0.3	0.6	< 0.1	< 0.1	0.2	0.1	–	–	–	< 0.1	–	–
Ag	< 0.1	< 0.1	< 0.1	0.1	< 0.1	< 0.1	–	–	–	< 0.1	–	–
Au	< 0.5	< 0.5	6.6	8.8	2.8	1.8	–	–	–	< 0.5	–	2.7
Hg	0.04	0.04	< 0.01	0.01	0.1	< 0.01	–	–	–	< 0.01	–	–
Tl	< 0.1	< 0.1	< 0.1	< 0.1	< 0.1	< 0.1	0.16	0.05	0.50	0.88	0.55	–
Se	< 0.5	< 0.5	< 0.5	< 0.5	< 0.5	2	–	–	–	< 0.5	–	–

halloysite tubes are quite long (1000–2000 nm), but the tube diameters (< 100 nm) are small. The morphology and dimensions of the halloysite can be related to the chemical compositions of the tubes. A suggestion by Bailey (1993) was that long tubes are generally rich in $A1_2O_3$ but poor in Fe_2O_3. The weathering of feldspar crystals and the formation of short (<500 nm) and thick (>100 nm) halloysite crystals were observed in the upper-level samples of the hanging wall block in DKD (Fig. 6c, d). These images revealed the halloysitization of the feldspars quite clearly.

The coexistence of euhedral (<30 μm) and spherical quartz (<30 μm) crystals was observed in the FE-SEM analysis of CKD (Fig. 5g, h). This morphological difference in the quartz crystals indicates that quartz polymorphs occurred under different physicochemical conditions and may be non-contemporary (Ercan et al., 2022). Spherical opal morphologies are cited as immature quartz. Below the vadose zone, opal transforms to chalcedony over time, and again with the effect of time, chalcedony transforms into coarse crystalline quartz (Hedenquist et al., 2000; Sillitoe, 1993, 2015).

Evaluation of the regional environment from the general mineralogical composition of the quarries is very important in order to understand the effective hydrothermal alteration processes of the study area and surrounding Etili. The XRD and FE-SEM analyses indicated that BKD, CKD, and DKD are composed mainly of kaolinite, halloysite, alunite, and quartz. All these minerals are commonly associated with advanced argillic alteration assemblages at lower temperatures and these are considered the basic mineral assemblage related to acid-sulfate geothermal fluids. The mineral groups in all of the kaolin deposits indicate a high-sulfidation environment under acidic (pH 2–4) conditions (Dill et al., 2005; Ece et al., 2008, 2013; Hedenquist et al., 2000; Pirajno, 2012). Kaolinite and alunite-group minerals are acid-stable in low-temperature environments above the groundwater table (Sillitoe, 1993). Alunite and kaolin in association occur typically under highly acidic and oxidizing conditions in a high-sulfidation

https://doi.org/10.1007/s42860-022-00214-4 Published online by Cambridge University Press

Table 3 $\delta^{18}O$ and δD isotopic content of kaolinite and calculated model formation temperature, assuming the $\delta^{18}O$ value of meteoric water to be –8‰ (Baba & Gunduz, 2010). $\delta^{34}S$ isotopic content of alunite and $^{40}Ar/^{39}Ar$ dating analyses from the alunite minerals in the study area

Sample ID	Mineral	$\delta^{34}S$ (VCDT)	$^{40}Ar/^{39}Ar$	
B2-8	Alunite	19.8	32.4 ± 1.2 (this study)	
B2-9	Alunite	20.2	32.2 ± 1.0 (this study)	
DU-1 (Footwall upper levels)	Alunite	10.5		
DC-1 (Footwall middle levels)	Alunite	–15.3		
DC-2 (Footwall middle levels)	Alunite	–17.2		
DC-3 (Footwall middle levels)	Alunite	–16.8		
DC-4 (Footwall middle levels)	Alunite	–17.2		
DA-1 (Hanging wall)	Alunite	0.9	29.7 ± 0.1 (this study)	
DA-2 (Hanging wall)	Alunite	–1.7		
M3	Natroalunite	16.6		
M28	Natroalunite	9.2		
CAL-2	Natroalunite	16.8	22.6 ± 0.2 (Ercan et. al.. 2022)	
CAL14	Natroalunite	15.4	28.5 ± 0.4 (Ercan et. al.. 2022)	
CAL2-4	Natroalunite	11.4		
CAL2-5	Natroalunite	5.7		
Galena	Galena	–0.3		
Pyrite	Pyrite	–0.1		
		$\delta^{18}O$ (VSMOW)	δD (VSMOW)	Model formation temperature (ºC)
BH-1	Kaolinite	11.8	–93	72
BH-6	Kaolinite	17.0	–99	39
B9	Kaolinite	16.7	–93	40
Çal-10	Kaolinite	12.2	–77	69
Çal-2	Kaolinite	10.3	–49	84
Çal-2–5	Kaolinite	11.4	–82	75
D13 (Footwall upper levels)	Kaolinite	14.5	–97	54
D14 (Footwall upper levels)	Kaolinite	13.6	–87	59
D-20-g (Footwall lower levels)	Kaolinite	14.4	–94	54
D-20-c (Footwall lower levels)	Kaolinite	15.0	–71	50
D-20-e (Footwall lower levels)	Kaolinite	14.1	–102	57
D-20-f (Footwall lower levels)	Kaolinite	15.2	–91	49
D2 (Hanging wall)	Kaolinite	13.3	–101	61
D6 (Hanging wall)	Kaolinite	15.1	–92	50
D8 (Hanging wall)	Kaolinite	18.3	–70	32
D9a (Footwall middle levels)	Kaolinite	16.3	–84	43
D9c (Footwall middle levels)	Kaolinite	13.3	–101	61

environment (Berger & Henley, 1989; Hedenquist et al., 2000). In this environment of formation, the pH of the steam-heated acid-sulfate fluids is ~2–3 and the presence of hydrochloric acid appears to be a source of this acidity (Schoen et al., 1974). Fluids in the pH 2–3 range can dissolve minerals such as volcanic glass, feldspar, and mica but not secondary kaolinite and alunite group minerals because Al is insoluble over these pH ranges (Schoen et al., 1974; Sillitoe, 1993). All the above-mentioned research indicates that the kaolin deposits with associations rich in kaolin + alunite minerals are formed by the effect of

https://doi.org/10.1007/s42860-022-00214-4 Published online by Cambridge University Press

steam-heated, acid sulfate fluids with low pH. Smectite + halloysite + feldspar associations are determined at the upper levels of the BKD and upper and middle levels of the DKD. These minerals represent neutral alkali-chloride conditions overlain by a steam-heated, acid-sulfate environment (Simon et al., 2005). Halloysite, smectite, and illite assemblages indicate pH 5 to 6 in the modern geothermal systems; such mineral associations suggest, therefore, that hydrothermal fluids had been neutralized vertically through interaction with the host rock (Reyes, 1990).

Geochemical Characterization of Quarries

The major oxide contents of the samples taken from the BKD, CKD, and DKD are different from each other, and this difference was evident in the SiO_2 contents (Table 2). Silica-rich fluids, which are the end members of alkali-chlorine hydrothermal fluids in epithermal systems, precipitate as SiO_2 in the pores and fractures of the rocks when they reach high saturation while moving through the rocks or along fracture zones. Previous research in this region revealed that an intense silicification generally occurs in the region (Ercan et al., 2022). Therefore, the high SiO_2 content in the samples can be associated with silicification. The SiO_2/Al_2O_3 ratio is between 2.69 and 5.11 for the BKD, 2.7 to 3.2 for the CKD, and 1.23 to 3.35 for the DKD; these ratios are far from an ideal kaolinite value (0.992–1.082). Because the kaolinite crystal forms matched the ideal kaolinite form in FE-SEM and XRD analysis, these high rates were interpreted as a silicification effect. The enrichment in Fe_2O_3 in the samples was interpreted as the precipitation of Fe-rich minerals from the epithermal solution enriched with FeO as a result of alteration of iron-rich minerals when suitable physicochemical conditions were encountered. The amounts of the other major and trace elements in the total mass decreased with the increase in the amount of SiO_2 related to silicification.

The main fractionation in the major oxide composition in and around the study area was influenced by the altered mineral associations of the host rock. The alteration of K-feldspar, plagioclase, biotite, hornblende, and matrix resulted in enrichment of Al, Si, Fe, Mg, and K in the solution and kaolinization occurred in the acidic open hydrological system, while in an immobile and slightly alkaline environment ‘smectitization’ took place (Erkoyun et al., 2019). Kaolinite and alunite minerals are compatible with the characteristic alteration products of the BKD, CKD, and DKD hydrothermal system. These indicate that the chemistry and pH of hydrothermal fluids changed spatially and temporally from acid-sulfate (kaolin group minerals) and slightly alkaline (smectite) to alkali-chloride solutions (silica sinter and silicification processes). The increment of K/(Ca + Na) ratio associated with S and Al indicates the formation of alunite under acidic environmental conditions, compatible with those reported in western and central Anatolia (Çelik Karakaya et al., 2021; Ece & Schroeder, 2007; Ece et al., 2008; Kadir et al., 2014, 2022; Mutlu et al., 2005; Sayın, 2007). The alunite minerals are typical hypogene minerals that formed during the initial phase of kaolinite formations and were observed frequently in all kaolin deposits in the study area.

The Ba, Sr, Rb, and K contents are enriched in all three kaolin deposits. Ba and Sr are affected quite rapidly by acidic hydrothermal fluids where alteration processes were effective. The role of feldspars and mica in the alteration processes causes significant enrichment in Ba and Sr elements in the alteration product. Most altered volcanics display an apparent enrichment in large ion lithophile elements (LILE) and that they retain the magmatic-arc volcanic origin (Ece & Schroeder, 2007). For LILE enrichment of the altered rocks, K-feldspar is recommended as a source mineral, if the geothermal solution is insufficiently saturated in deep reservoirs, K-feldspar hydrolyzes and as a result, the dissolution of K-feldspar changes the chemical composition of geothermal fluids, especially for the enrichment of LILE (Dill et al., 1997).The depletion of Ce, Y, and La, together with the negative Eu anomaly and enrichment in Sr and Ba, shows that the fractionation by feldspar and mica originated from volcano-sedimentary rocks during the magmatic and hydrothermal alteration processes and was the primary source for the formation of kaolinite and alunite (Kadir et al., 2022). Trace element values for the altered minerals at BKD, CKD, and DKD were determined using the studies of Dill et al. (1997). Most of the kaolin samples at BKD and CKD fell in the hypogene area, but the DKD samples fell in the supergene area (Fig. 7a). According to MacLean and Barrett (1993), in a $Zr–TiO_2$ binary diagram used to clarify the hypogene-supergene effects of kaolin deposits,

https://doi.org/10.1007/s42860-022-00214-4 Published online by Cambridge University Press

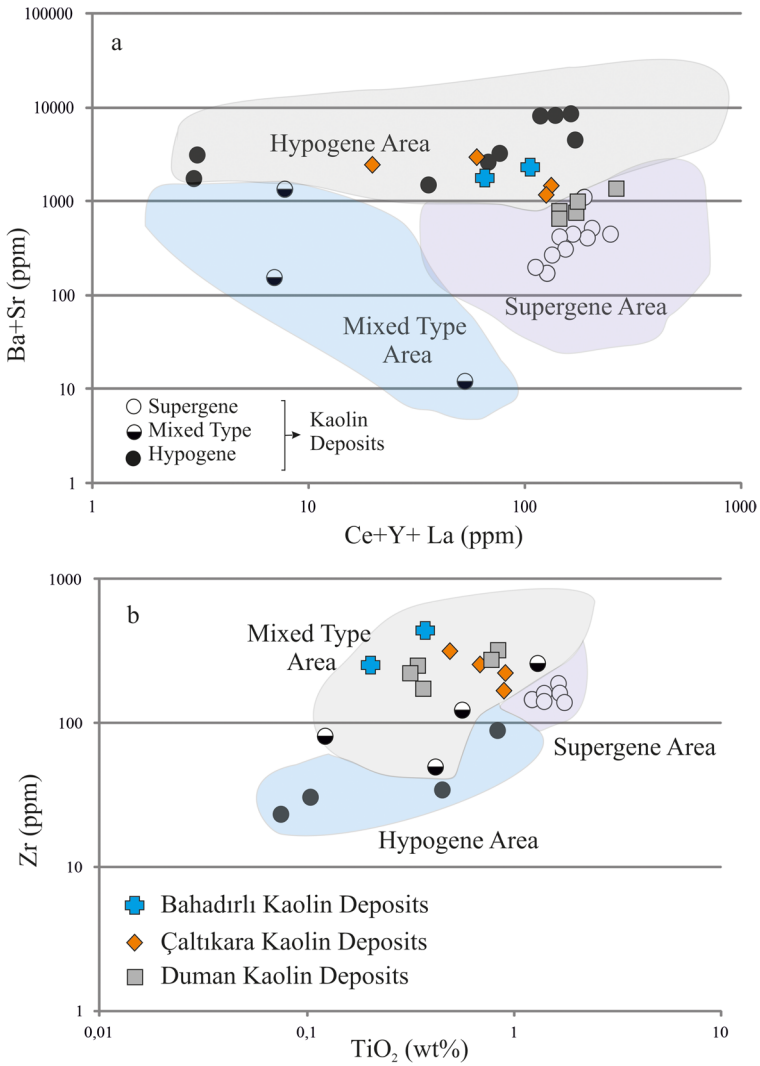

Fig. 7 **a** Ba + Sr/Ce + Y + La binary diagram and **b** Zr/TiO_2 binary diagram used for the determination of the origin of the acidic waters causing the formation of kaolinization in the Bahadırlı, Çaltıkara, and Duman kaolin deposits (modified from Dill et al., 1997)

all samples indicate a mixed-origin type (Fig. 7b). Projections, based on elemental data from these two binary graphs, indicate that all the altered samples from three kaolin deposits occurred under the effects of supergene and hypogene solutions. In addition, the DKD kaolins were more affected by the supergene solutions which can be related to waters of lacustrine origin (Fig. 7).

The REE contents of DKD are enriched compared to CKD and BKD (Fig. 8). The REEs are relatively insoluble; many studies have shown that REEs can be mobilized and can fractionate during the formation, deposition, and diagenesis of sediments and rocks, thereby providing a valuable geochemical tool for diagenetic studies of highly weathered materials (Cheshire et al., 2018). Ion adsorption-style deposits occur in the weathered crusts of granitic rocks where REE behaving as positively charged trivalent ions during weathering are considered to be adsorbed on negatively charged surfaces of clay minerals such as kaolinite and halloysite (Murakami & Ishihara, 2008). Under low ionic strength, as the REEs are adsorbed through ion exchange and surface complexation; the REE sorption capacity of kaolin and halloysite increases at high pH levels and they also adsorb REE in a similar ratio (Yang et al., 2019). For this reason, it

https://doi.org/10.1007/s42860-022-00214-4 Published online by Cambridge University Press

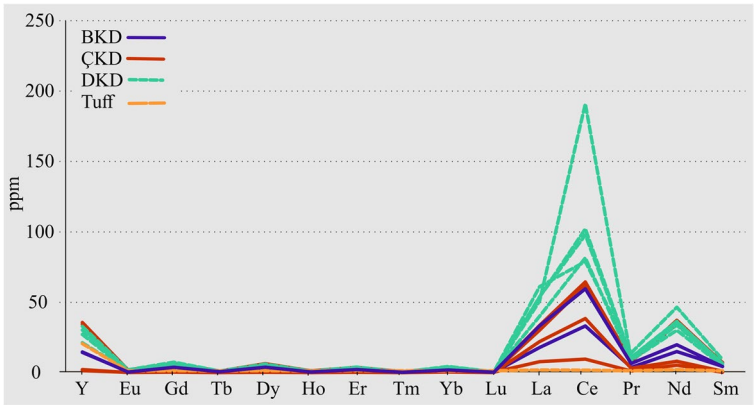

Fig. 8 Graphic showing REE contents of kaolin samples and tuff taken from Bahadırlı, Çaltıkara, and Duman quarries. Blue lines: Bahadırlı kaolinite, gray lines: Çaltıkara kaolinite, green lines: Duman kaolinite, red line: Tuff. Vertical axis: concentration (ppm)

is suggested that the probable formation environment of DKD had a higher pH than other kaolin deposits and, therefore, REE adsorption occurred more here than in the other two deposits. The high pH of the solution effective in this deposit was also suggested and supported by its mineralogical composition.

Stable Isotope Characterization of Quarries

The alunite $\delta^{34}S$ isotope values from all of the deposits are quite different from each other and the sulfur isotope data indicate at least three different environments of formation. The $\delta^{34}S$ isotope values of the galena and pyrite samples ranged from –0.1 to –0.3‰ and two alunite samples from the hanging wall block of the DKD ranged from –1.7 to 0.9‰ (Table 3). These pointed to a magmatic-hydrothermal sulfur source (–3 ± 3%; Rye et al., 1992). However, the $\delta^{34}S$ values in alunite were depleted at the footwall blocks samples of the DKD. The $\delta^{34}S$ isotope values ranged from –15.3 to –17.2‰ for this block, indicating the presence of reduced sulfur produced by a microbial reducing environment or a sedimentary source for sulfur (Cunningham et al., 1984, 2005) (Table 3). In the case of oxidation of the starting material in sulfur redox processes, the product formed becomes enriched in $\delta^{34}S$, while reduction causes the formation of products depleted in $\delta^{34}S$ (Seal et al., 2000). Sulfate-reducing bacteria are found mostly in anoxic media such as below the sediment–water interface and in anoxic water bodies. These bacteria can stay alive in the temperature range 0 to 110°C and pH conditions of 5 to 9.5 (Postgate, 1984). The data indicating this high-pH environment are consistent with the interpretations about the environment obtained from the mineralogical and chemical data of the DKD. The BKD, CKD, and DKD (DU-1, representing the upper levels of the footwall block) samples were enriched in $\delta^{34}S$, with very large positive values being attained (Table 3). During pyrite precipitation by bacterial reduction of sulfate, $\delta^{32}S$ was enriched in the sulfide, which caused enrichment of $\delta^{34}S$ in the residual sulfate-rich solution; therefore, secondary sulfate minerals are enriched in $\delta^{34}S$ (Seal et al., 2000). Ercan et al. (2022) suggested that the organic acid input may result from the interaction of lacustrine coal deposits with groundwater/geothermal fluids, observed commonly in the study area. In addition, the detection of retiform structures of microfossils in micromorphological studies ((supplementary material Table S1, ESM-1pdf)) also supported the possibility of the existence of bio-organism activities in this quarry.

$\delta^{18}O$ versus δD isotopic values of the BKD fall on the kaolinite line (two samples) and halloysite line (one sample) and also kaolinite $\delta^{18}O$ versus δD isotopic values of the DKD fall between the kaolinite and halloysite lines (Fig. 7). The $\delta^{18}O$ and δD isotopic values of CKD are very close to the supergene/hypogene line proposed by Sheppard and Gilg (1996) (Fig. 9) and only one kaolinite sample falls near the magmatic water area. Although $\delta^{18}O$ and δD isotope values of all CKD kaolins indicated a hypogene origin, kaolin samples from BKD and CKD indicate a supergene origin. All of these isotope data are very consistent with and

https://doi.org/10.1007/s42860-022-00214-4 Published online by Cambridge University Press

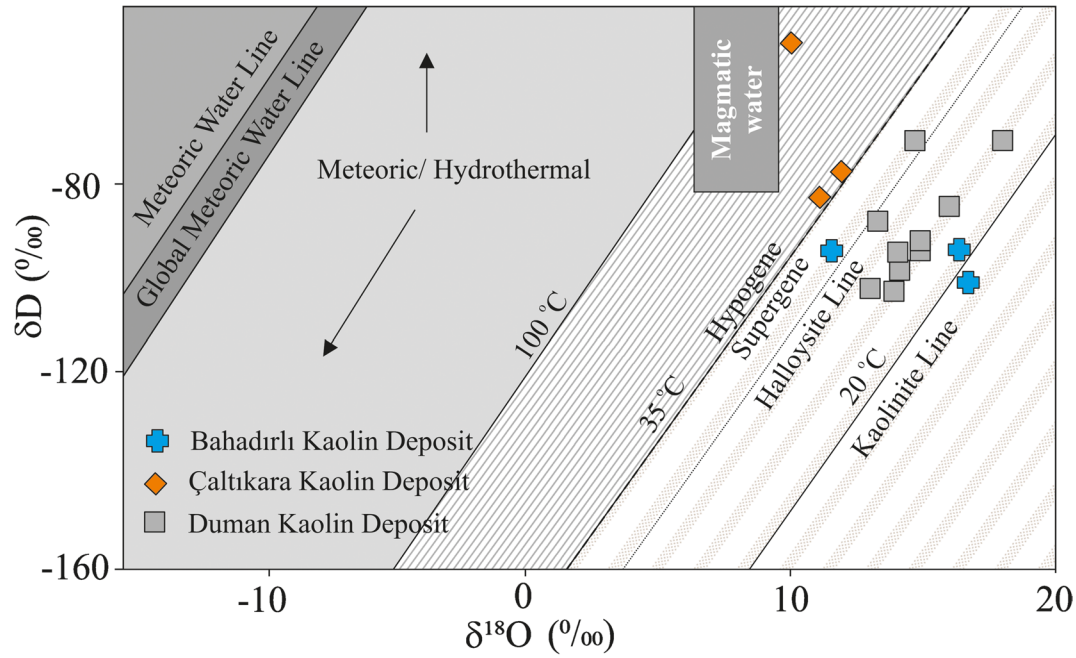

Fig. 9 The $\delta^{18}O$ and δD binary diagram. The $\delta^{18}O$ and δD isotopic values of kaolins from the Bahadırlı, Çaltıkara, and Duman kaolin deposits, hydrothermal kaolins from active geothermal fields, and thermal waters near kaolin locations in Japan (Hayba et al., 1985). The meteoric water line is $\delta D = 6.8 * \delta^{18}O + 10.5$ (Harris et al., 1999). Supergene vs. hypogene (S/H) lines are taken from Sheppard and Gilg (1996). Equilibrium lines for kaolinite and halloysite at various temperatures were calculated assuming meteoric water of $\delta^{18}O = -8‰$ for the Kirazlı region of Çanakkale; this value is taken from Baba and Gunduz et al. (2010)

confirm the formation environment results obtained from trace-element data. In addition, the isotopic data revealed clearly that DKD was more affected by hypogene origin solutions, but DKD was more exposed to supergene effects. The calculated model temperatures of the CKD range from 69 to 84ºC, these values reflecting temperatures of the fossil geothermal fields. The CKD probably formed in a hypogene environment and isotopic data plot very close to the line representing kaolinites in equilibrium with meteoric waters at 35ºC. These lower temperatures were then possibly related to a steam-heated process, which condensed waters in the vadose zone, mixed with meteoric water, and then isotopically re-equilibrated (Ercan et al., 2016).

The area to the left of the S/H line indicates a hypogene origin for the CKD, whereas the areas to the right-hand side indicate a supergene environment for the BKD and DKD. Component-calculated model formation temperatures of the BKD and DKD deposit are between 40–72ºC and 32–61ºC, respectively, thus reflecting isotopic equilibrium with meteoric water in the supergene environment (Table 3).

The consensus is that calc-alkaline plutonism was active from Early Eocene to Early Miocene and hydrothermal alterations were active from Late Eocene through Miocene. The findings of $^{40}Ar/^{39}Ar$ alunite dates (22.6 ± 0.2 to 32.4 ± 1.2 Ma) (Table 3) are consistent with the alteration dates of primary volcanic rocks (29.7 to 32.4 Ma) (Altunkaynak & Yılmaz, 1998; Altunkaynak et al., 2012; Altunkaynak & Dilek, 2013; Buyukkahraman & Çoban, 2013; Ercan et al., 2016; Ercan et al., 2022; Özdamar, 2021b; Yılmaz & Karacık, 2001). Consequently, radiometric dating in the region revealed that the active period of calc-alkaline plutonism and the alteration processes due to hydrothermal activity were highly correlated and occurred at approximately the same time. These dates indicate that the alunite at BKD and CKD probably formed during igneous hydrothermal activity, but the isotopic studies of DKD revealed that, besides the hydrothermal activity, groundwater was mixed with organic acid derived from the coal deposits of lacustrine origin. Because the amount of alunite collected from the CKD was insufficient, $^{40}Ar/^{39}Ar$ dating was

https://doi.org/10.1007/s42860-022-00214-4 Published online by Cambridge University Press

not carried out, but the dating obtained from the south of this deposit (Ercan et al., 2022) was in the range 22.6–28.5 Ma. These data are compatible with the dating of DKD and BKD quarries which are located along the same fault.

Conclusions

Data from the mineral assemblages and chemical and isotopic compositions of the Bahadırlı, Çalıkara, and Duman kaolin deposits can be used to help distinguish between supergene and hypogene origins in hydrothermal kaolin deposits. Based on two different mineral assemblages of alteration groups, two different hydrothermal stages were proposed for the region. In the first stage, representing BKD, CKD, and the hanging-wall side of DKD, highly acidic and oxidizing conditions prevailed, as shown by the presence of alunite and kaolinite, an indicator of high-temperature mineralization, formed in relatively deep epithermal zones (Berger & Henley, 1989; Hedenquist et al., 2000; Sillitoe, 1993). During the second stage, which is represented by the middle and upper levels of the DKD, kaolinite, smectite, and halloysite were formed and some of the original textures of the tuffs were destroyed due to lower intensity chemical reactions of geothermal acids, organic humic acids, and meteoric waters. The mixture of groundwater and/or geothermal waters and humic acid fluids during the alteration in DKD was also supported by isotopic data. In this study, humic acids are suggested teo originate from lacustrine coal deposits, which are commonly observed in the Etili region (Table 4).

During the Oligocene–Early Miocene to Middle and Upper Miocene, the evolution of alteration processes and hydrothermal fluids in the region is shown clearly in the footwall block of the DKD. The footwall blocks of the DKD reflect the mineralogical, chemical, and isotopic properties dominated by the effect of acid-sulfate hydrothermal fluids at the base. However, the mineralogical composition, geochemical properties, and ^{34}S isotope characterization of the samples of the upper zones of the footwall block revealed the hypogene-supergene transition with the effect of the alkali-chloride fluids.

This study revealed that three kaolin deposits located in the same host rock and very close to each other in the Çanakkale Region experienced different stages and degrees of hydrothermal alteration processes. Each deposit was presumably affected by the groundwater and meteoric waters differentially heated

Table 4 Determination of hypogene and supergene alteration criteria of kaolin deposits in the Etili region

Distinguishing criteria	Bahadırlı KD	Duman KD	Çaltıkara KD
Altered minerals association	Kaolinite, alunite, halloysite, quartz, montmorillonite, illite	Halloysite, kaolinite, alunite, natroalunite illite, montmorillonite	Quartz, kaolinite, alunite, halloysite, natroalunite, iron oxide, sulfide minerals
Kaolinite crystal habits	Blocky, booklet stacks	Equidimensional and booklet stacks	Equidimensional randomly oriented
Halloysite crystal habits	Well-formed tubes	Well-formed, long and thin tubes	Short poorly tubes
Alunite crystal habits	Euhedral <10 µm with dissolution pits	Earthy	Euhedral <5 µm
Feldspar crystal habits	Advanced stage of formation of kaolinite crystals	Well-formed with dissolution pits and early stage of formation of halloysite tubes	Advanced stage of formation of kaolinite crystals
Quartz crystal habits	Euhedral	Euhedral	Euhedral 30 µm and spherical quartz
Silica content	Abundant within the fault zone	Poor	Abundant within fault zones
(Ba + Sr) vs. (Ce + Y + La)	Hypogene area	Supergene area	Hypogene area
Zr vs.TiO_2	Mixed type area	Mixed-type area	Mixed-type area
$\delta^{18}O$ vs δD of kaolins	$\delta^{18}O$ enrichment, slight δD depletion	$\delta^{18}O$ enrichment, δD enrichment	$\delta^{18}O$ depletion, δD enrichment
$\delta^{34}S$ of alunites	$\delta^{34}S$ enrichment	Mostly $\delta^{34}S$ depletion	$\delta^{34}S$ enrichment

https://doi.org/10.1007/s42860-022-00214-4 Published online by Cambridge University Press

by hydrothermal processes. The BKD, CKD, and DKD quarries are very close to each other, offer many different mineralogical, geochemical, and isotopic data, and can be used as a guide in solving and understanding the origin of similar formations throughout the world.

Acknowledgements The authors are grateful to ITU-JAL labs for providing analytical support during geochemical analysis in ITU, Turkey. They also thank the Kalemaden Mining Corp. for logistical support and accommodation during the fieldwork.

Funding This research was supported by TUBITAK Project No: 112Y369 (Project coordinator: Prof. Dr. Ömer Işık Ece).

Data Availability All data related to the manuscript are presented in tables.

Code availability Not applicable.

Credit authorship contribution statement: Hatice Ünal Ercan: Conceptualization, investigation, writing—original draft, writing—review and editing, visualization. Ömer Işık Ece: Conceptualization, investigation, writing—review and editing, project administration, funding acquisition. Emin Çiftçi: Conceptualization, investigation, writing—review and editing. Ayça Aydın: Investigation, formal analysis, review and editing.

Declarations

Conflicts of Interest The authors certify that they have no affiliations with or involvement in any organization or entity with any financial interest or non-financial interest in the subject matter or materials discussed in this manuscript.

References

Ağdemir, N., Kırıkoğlu, M. S., Lehmann, B., & Tietze, J. (1994). Petrology and alteration geochemistry of the epithermal Balya Pb–Zn–Ag deposit, NW Turkey. *Mineralium Deposita, 29*, 366–371.

Aldanmaz, E., Pearce, J. A., Thirlwall, M. F., & Mitchell, J. G. (2000). Petrogenic evolution of Late Cenozoic, post-collisional volcanism in western Anatolia, Turkey. *Journal of Volcanology and Geothermal Research, 102*, 67–95.

Altunkaynak, S., & Dilek, Y. (2006). Timing and nature of post-collisional volcanism in western Anatolia and geodynamic implications. *Special Papers - Geological Society of America, 409*, 321.

Altunkaynak, Ş, & Dilek, Y. (2013). Eocene mafic volcanism in northern Anatolia: Its causes and mantle sources in the absence of active subduction. *International Geology Review, 55*(13), 1641–1659.

Altunkaynak, Ş, & Genç, S. C. (2008). Petrogenesis and time-progressive evolution of the Cenozoic continental volcanism in the Biga Peninsula, NW Anatolia (Turkey). *Lithos, 102*, 316–340.

Altunkaynak, Ş, & Yılmaz, Y. (1998). The mount Kozak magmatic complex, western Anatolia. *Journal of Volcanology and Geothermal Research, 85*(1–4), 211–231.

Altunkaynak, Ş, Sunal, G., Aldanmaz, E., Genç, C. Ş, Dilek, Y., Furnes, H., & Yıldız, M. (2012). Eocene granitic magmatism in NW Anatolia (Turkey) revisited: New implications from comparative zircon SHRIMP U-Pb and $^{40}Ar/^{39}Ar$ geochronology and isotope geochemistry on magma genesis and emplacement. *Lithos, 155*, 289–309.

Aydın, A. (2014). *Çan-Çanakkale bölgesi kaolinit yataklarının ve çevresinin petrografik mineralojik ve jeokimyasal incelenmesi (MS Thesis* (p. 107). Istanbul Technical University.

Aydın, Ü. (2019). Biga Yarımadası'ndaki granitoyitlerin (KB Anadolu, Türkiye) petrolojik ve jeokimyasal özellikleri. *Maden Tetkik Arama Dergisi, 160*, 81–116.

Baba, A., & Gunduz, O. (2010). Effect of alteration zones on water quality: A case study from biga peninsula, Turkey. *Archives of Environmental Contamination and Toxicology, 58*(3), 499–513.

Bailey, S. W. (1993). Review of the structural relationships of the kaolin minerals. In H. H. Murray, W. M. Bunday, & C. C. Harvey (Eds.), *Kaolin Genesis and Utilization Boulder, Colorado, USA 1, 25–42*. Clay Minerals Society Special Publication.

Barnes, H. L., & Seward, T. M. (1997). Geothermal systems and mercury deposits. *Geochemistry of Hydrothermal Ore Deposits, 3*, 699–736.

Beaufort, D., Cassagnabere, A., Petit, S., Lanson, B., Berger, G., Lacharpagne, J. C., & Johansen, H. (1998). Kaolinite-to-dickite reaction in sandstone reservoirs. *Clay Minerals, 33*(2), 297–316.

Berger, B.R., & Henley, R.W. (1989). Advances in the understanding of epithermal gold-silver deposits, with special reference to the western United States. *Economic Geology Monograph, 6*. https://doi.org/10.5382/Mono.06.32

Birkle, P., & Satır, M. (1995). Dating, geochemistry and geodynamic significance of the tertiary magmatism of the Biga Peninsula, NW-Turkey. Geology of the Black Sea Region. In A. Erler, T. Ercan, E. Bingöl, S. Örçen (Eds.), Geology of the Black Sea Region (pp. 171–180). MTA.

Buyukkahraman, G., & Coban, F. (2013). Mineralogical-geochemical characteristics and genetic implication of Gumeli (Ivrindi, BALIKESIR) Talc occurrences in the Karakaya complex (NW Turkey). *European Scientific Journal, 9*(33).

Çelik Karakaya, M., Karakaya, N., Temel, A., & Yavuz, F. (2021). Mineralogical and geochemical properties and genesis of kaolin and alunite deposits SE of Aksaray (Central Turkey). *Applied Geochemistry, 124*, 104830.

Cheshire, M. C., Bish, D. L., Cahill, J. F., Kertesz, V., & Stack, A. G. (2018). Geochemical evidence for rare-earth element mobilization during kaolin diagenesis. *ACS Earth and Space Chemistry, 2*(5), 506–520.

Çiçek, M., Oyman, T., & Palmer, M. R. (2021). Variation of Cu, Fe, S and Pb isotopes in sulfides from hydrothermal mineralization from the Yenice region in Çanakkale, Biga Peninsula. *NW Turkey. Ore Geology Reviews, 136*, 104255.

Cooke, D. R., & Simmons, S. F. (2000). Characteristics and genesis of epithermal gold deposits. *Society of Economic Geology Reviews, 13*, 221–244.

Cunningham, C. G., Rye, R. O., Steven, T. A., & Mehnert, H. H. (1984). Origins and exploration significance of replacement and vein-type alunite deposits in the Marysvale volcanic field, west central Utah. *Economic Geology, 79*(1), 50–71.

Cunningham, C. G., Rye, R. O., Rockwell, B. W., Kunk, M. J., & Councell, T. B. (2005). Supergene destruction of a hydrothermal replacement alunite deposit at Big Rock Candy Mountain, Utah: Mineralogy, spectroscopic remote sensing, stable-isotope, and argon-age evidences. *Chemical Geology, 215*(1–4), 317–337.

Delaloye, M., & Bingol, E. (2000). Granitoids from Western and Northwestern Anatolia: Geochemistry and modeling of geodynamic evolution. *International Geology Review, 42*, 241–268.

Dewey, J. F., & Şengör, A. C. (1979). Aegean and surrounding regions: Complex multiplate and continuum tectonics in a convergent zone. *Geological Society of America Bulletin, 90*(1), 84–92.

Dill, H. G. (2016). Kaolin: Soil, rock and ore: From the mineral to the magmatic, sedimentary and metamorphic environments. *Earth-Science Reviews, 161*, 16–129.

Dill, H. G., & Horn, E. E. (1996). The origin of a hypogene sarabauite-calcite mineralization at the Lucky Hill Au-Sb mine Sarawak, Malaysia. *Journal of Southeast Asian Earth Sciences, 14*(1–2), 29–35.

Dill, H. G., Bosse, H. R., Henning, K. H., & Fricke, A. (1997). Mineralogical and chemical variations in hypogene and supergene kaolin deposits in a mobile fold belt the Central Andes of Northwestern Peru. *Mineralium Deposita, 32*, 149–163.

Dill, H. G., Botz, R., & Luppold, F. W. (2005). Hypogene and supergene alteration of the Late Palaeozoic Ratburi Limestone during the Mesozoic and Cenozoic (Thailand, Surat Thani Province). Implications for the concentration of mineral commodities and hydrocarbons. *International Journal of Earth Sciences, 94*, 24–46.

Ece, O. I., & Schroeder, P. A. (2007). Clay mineralogy and chemistry of halloysite and alunite deposits in the Turplu area, Balikesir, Turkey. *Clays and Clay Minerals, 55*(1), 18–35.

Ece, O. I., Schroeder, P. A., Smilley, M. J., & Wampler, J. M. (2008). Acid-sulphate hydrothermal alteration of andesitic tuffs and genesis of halloysite and alunite deposits in the Biga Peninsula, Turkey. *Clay Minerals, 43*, 281–315.

Ece, O. I., Ekinci, B., Schroeder, P. A., Crowe, D., & Esenli, F. (2013). Origin of the Düvertepe kaolin–alunite deposits in Simav Graben, Turkey: Timing and styles of hydrothermal mineralization. *Journal of Volcanology and Geothermal Research, 255*, 57–78.

Ercan, T., Satir, M., Steinitz, G., Dora, A., Sarifakioglu, E., Adis, C., Walter, H. J., & Yildirim, T. (1995). Features of Tertiary volcanism observed at Biga Peninsula and Gökçeada, Tavsan Islands, NW Anatolia. *Bulletin of the Mineral Research and Exploration, 117*, 55–86. (in Turkish).

Ercan, H. Ü., Ece, Ö. I., Schroeder, P. A., & Karacik, Z. (2016). Differentiating styles of alteration within kaolin-alunite hydrothermal deposits of Çanakkale NW Turkey. *Clays and Clay Minerals, 64*(3), 245–274.

Ercan, H. Ü., Ece, Ö. I., Schroeder, P. A., & Gülmez, F. (2022). Characteristics and evolution of the Etili silica sinter epithermal deposits, Çanakkale–Turkey: Relation to alkali chloride vs acid-sulfate fluids. *Ore Geology Reviews, 142*, 104726.

Erenoğlu, O. (2017). Çan taşı tüfü'nün mineralojik özellikleri ve jeokronolojisi (Biga Yarımadası, KB Türkiye). *Türkiye Jeoloji Bülteni, 60*(3), 433–449.

Erkoyun, H., Kadir, S., & Huggett, J. (2019). Occurrence and genesis of tonsteins in the Miocene lignite, Tunçbilek Basin, Kütahya, western Turkey. *International Journal of Coal Geology, 202*, 46–68.

Genç, ŞC. (1998). Evolution of the Bayramiç magmatic complex, northwestern Anatolia. *Journal of Volcanology and Geothermal Research, 85*(1–4), 233–249.

Harris, C., Compton, J. S., & Bevington, S. A. (1999). Oxygen and hydrogen isotope composition of kaolinite deposits, Cape Peninsula, South Africa: Low-temperature, meteoric origin. *Economic Geology, 94*, 1353–1366.

Hayba, D. O., Bethke, P. M., Heald, P., & Foley, N. K. (1985). Geologic, mineralogic, and geochemical characteristics of volcanic-hosted epithermal precious metal deposits. Pp 129–167 in Geology and Geochemistry of Epithermal Systems (B.R. Berger and P.M. Bethke, editors). *Reviews in Economic Geology, 2*, 250–252.

Hedenquist, J. W., Arribas, A., & Gonzalez-Urien, E. (2000). Exploration for epithermal gold deposits. *Reviews in Economic Geology, 13*(2), 45–77.

Hemley, J. J., Meyer, C., Hodgson, C. J., & Thatcher, A. B. (1967). Sulfide solubilities in alteration-controlled systems. *Science, 158*(3808), 1580–1582.

Hillier, S., Brydson, R., Delbos, E., Fraser, T., Gray, N., Pendlowski, H., & Wilson, I. (2016). Correlations among the mineralogical and physical properties of halloysite nanotubes (HNTs). *Clay Minerals, 51*(3), 325–350.

Jolivet, L., & Brun, J. P. (2010). Cenozoic geodynamic evolution of the Aegean. *International Journal of Earth Sciences, 99*(1), 109–138.

Jolivet, L., & Faccenna, C. (2000). Mediterranean extension and the Africa-Eurasia collision. *Tectonics, 19*, 1095–1106.

Jolivet, L., Faccenna, C., Huet, B., Labrousse, L., Le Pourhiet, L., Lacombe, O., & Philippon, M. (2013a). Aegean tectonics: Strain localisation, slab tearing and trench retreat. *Tectonophysics, 597*, 1–33.

Jolivet, L., Faccenna, C., Huet, B., Labrousse, L., Le Pourhiet, L., Lacombe, O., & Driussi, O. (2013b). Aegean tectonics: Strain localisation, slab tearing and trench retreat. *Tectonophysics, 597*, 1–33.

Justet, L., & Spell, T. L. (2001). Effusive eruptions from a large silicic magma chamber: The Bearhead Rhyolite, Jemez volcanic field, NM. *Journal of Volcanology and Geothermal Research, 107*, 241–264.

Kadir, S., Külah, T., Eren, M., Onalgil, N., & Gürel, A. (2014). Mineralogical and geochemical characteristics and genesis of the Güzelyurt alunite-bearing kaolinite deposit within the late Miocene Gördeles ignimbrite, central Anatolia, Turkey. *Clays and Clay Minerals, 62*, 477–499.

Kadir, S., Ateş, H., Erkoyun, H., Külah, T., & Esenli, F. (2022). Genesis of alunite-bearing kaolin deposit in Mudamköy, member of the Miocene Göbel Formation, Mustafakemalpaşa (Bursa). *Turkey. Applied Clay Science, 221*, 106407.

Karacık, Z., & Yılmaz, Y. (1998). Geology of the ignimbrites and the associated volcano–plutonic complex of the Ezine area, northwestern Anatolia. *Journal of Volcanology and Geothermal Research, 85*(1–4), 251–264.

Karacık, Z., Yılmaz, Y., Pearce, J. A., & Ece, O. I. (2008). Petrochemistry of the south Marmara granitoids, northwest Anatolia. *Turkish Journal of Earth Sciences, 97*, 1181–1200.

Kaymakci, N., Aldanmaz, E., Langereis, C., Spell, T. L., Gurer, O. F., & Zanetti, K. A. (2007). Late Miocene transcurrent tectonics in NW Turkey: Evidence from paleomagnetism and ^{40}Ar-^{39}Ar dating of alkaline volcanic rocks. *Geological Magazine, 144*(2), 379–392.

Laçin, D., Aysal, N., & Öngen, S. (2021). Geological mineralogical and technological properties of Oligocene-Miocene clay deposits in altered volcanic rocks for the ceramic industry (Western Anatolia, Turkey). *Arabian Journal of Geosciences, 14*(18), 1–16.

Le Pichon, X., Imren, C., Rangin, C., Şengör, A. C., & Siyako, M. (2014). The South Marmara Fault. *International Journal of Earth Sciences, 103*(1), 219–231.

Lindgren, W. (1933). *Mineral Deposits* (4th ed., p. 930). McGraw Hill.

Lueth, V. W., Megaw, P. K., Pingitore, N. E., & Goodell, P. C. (2000). Systematic variation in galena solid-solution compositions at Santa Eulalia, Chihuahua, Mexico. *Economic Geology, 95*(8), 1673–1687.

MacLean, W. H., & Barrett, T. J. (1993). Lithogeochemical techniques using immobile elements. *Journal of Geochemical Exploration, 48*(2), 109–133.

Moore, D. M., & Reynolds Jr, R. C. (1989). *X-ray diffraction and the identification and analysis of clay minerals*. Oxford University Press (OUP).

Murakami, H., & Ishihara, S. (2008). REE mineralization of weathered crust and clay sediment on granitic rocks in the Sanyo Belt, SW Japan and the Southern Jiangxi Province China. *Resource Geology, 58*(4), 373–401.

Murray, H. H., & Keller, W. D. (1993). Kaolins, kaolins, and kaolins. In H. H. Murray, W. M. Bundy, & C. Harvey (Eds.), *Kaolin Genesis and Utilization.* Clay Minerals Society Special Publication. https://doi.org/10.1346/CMS-SP-1.1

Mutlu, H., Sarıiz, K., & Kadir, S. (2005). Geochemistry and origin of the Şaphane alunite deposit, western Anatolia, Turkey. *Ore Geology Reviews, 26*, 39–50.

Okay, A. I. (2001). Stratigraphic and metamorphic inversions in the central Menderes Massif: A new structural model. *International Journal of Earth Sciences, 89*(4), 709–727.

Okay, A. I., & Satir, M. (2000). Coeval plutonism and metamorphism in a latest Oligocene metamorphic core complex in northwest Turkey. *Geological Magazine, 137*(5), 495–516.

Oyman, T. (2010). Geochemistry, mineralogy and genesis of the Ayazmant Fe-Cu skarn deposit in Ayvalik, (Balikesir). *Turkey. Ore Geology Reviews, 37*(3–4), 175–201.

Oyman, T. (2019). *Epithermal Deposits of Turkey. In: Mineral Resources of Turkey Modern Approaches in Solid Earth Sciences, 159–223*. Springer. https://doi.org/10.1007/978-3-030-02950-0_4

Özdamar, Ş. (2018). Evciler Plütonu'nun (KB Türkiye) Petrolojisi. *Kahramanmaraş Sütçü İmam Üniversitesi Mühendislik Bilimleri Dergisi, 21*(2), 149–165.

Özdamar, Ş, Roden, M. F., Zou, H., Billor, M. Z., Hames, W., Georgiev, S., & Dunkl, I. (2021a). Petrogenesis of oligocene plutonic rocks in western Anatolia (NW Turkey): Insights from mineral and rock chemistry, Sr-Nd isotopes, and U-Pb, Ar-Ar and (U-Th)/He geochronology. *Geochemistry, 81*(2), 125747. https://doi.org/10.1016/j.chemer.2021.125747

Özdamar, Ş, Zou, H., Billor, M. Z., & Hames, W. E. (2021b). Petrogenesis of mafic microgranular enclaves (MMEs) in the Oligocene-Miocene granitoid plutons from northwest Anatolia. *Turkey. Geochemistry, 81*(2), 125713. https://doi.org/10.1016/j.chemer.2020.125713

Pirajno, F. (1995). Volcanic-hosted epithermal systems in northwest Turkey. *South African Journal of Geology, 98*(1), 13–24.

Pirajno, F. (2012). *Hydrothermal mineral deposits: Principles and fundamental concepts for the exploration geologist, 721 pp*. Springer Science and Business Media.

Postgate, J. R. (1984). *The Sulfate-Reducing Bacteria* (2nd ed., pp. 1–208). Cambridge Univ. Press.

Reyes, A. G. (1990). Petrology of Philippine geothermal systems and the application of alteration mineralogy to their assessment. *Journal of Volcanology and Geothermal Research, 43*(1–4), 279–309.

Rye, R. O., & Alpers, C. N. (1997). *The stable isotope geochemistry of jarosite (p. 28)*. US Department of the Interior. US Geological Survey.

Rye, R. O., Bethke, P. M., & Wasserman, M. D. (1992). The stable isotope geochemistry of acid sulfate alteration. *Economic Geology, 87*, 225255.

Sayın, S. A. (2007). Origin of kaolin deposits: Evidence from the Hisarcık (Emet-Kütahya) deposits, western Turkey. *Turkish Journal of Earth Science, 16*, 77–96.

Schoen, R., White, D. E., & Hemley, J. J. (1974). Argillization by descending acid at Steamboat Springs, Nevada. *Clays and Clay Minerals, 22*, 1–22.

Seal, R. R., Alpers, C. N., & Rye, R. O. (2000). Stable isotope systematics of sulfate minerals. *Reviews in Mineralogy and Geochemistry, 40*(1), 541–602.

Seyitoğlu, G., & Scott, B. C. (1996). The cause of NS extensional tectonics in western Turkey: Tectonic escape vs back-arc spreading vs orogenic collapse. *Journal of Geodynamics, 22*(1–2), 145–153.

Sheppard, S. M. F., & Gilg, H. A. (1996). Stable isotope geochemistry of clay minerals. *Clay Minerals, 31*, 1–24.

Sillitoe, R. H. (2015). Epithermal paleosurfaces. *Mineralium Deposita, 50*(7), 767–793.

Sillitoe, R. H., Hannington, M. D., & Thompson, J. F. (1996). High sulfidation deposits in the volcanogenic massive sulfide environment. *Economic Geology, 91*(1), 204–212.

Sillitoe, R. H. (1993). Gold-rich porphyry copper deposits: Geological model and exploration implications. In R. V. Kirkham, W. d. Sinclair, R. I. Thorpe, & J. M. Duke (Eds.), *Mineral Deposit Modeling: Geological*

Association of Canada, Special Paper (vol. 40, pp. 465–478).

Simon, A. C., Frank, M. R., Pettke, T., Candela, P. A., Piccoli, P. M., & Heinrich, C. A. (2005). Gold partitioning in melt-vapor-brine systems. *Geochimica et Cosmochimica Acta, 69*(13), 3321–3335.

Siyako, M., Bürkan, K. A., & Okay, A. I. (1989). Tertiary geology and hydrocarbon potential of the Biga and Gelibolu Peninsulas. *Türkiye Petrol Jeologları Derneği Bulletin, 1*(3), 183–199.

Skinner, B. J., & Barton, P. B., Jr. (1973). Genesis of mineral deposits. *Annual Review of Earth and Planetary Sciences, 1*(1), 183–211.

Spell, T. L., & McDougall, I. (2003). Characterization and calibration of $^{40}Ar/^{39}Ar$ dating standards. *Chemical Geology, 198*, 189–211.

Staudacher, T., Jessberger, E. K., Dorflinger, D., & Kiko, J. (1978). A refined ultra-high vacuum furnace for rare gas analysis. *Journal of Physics E: Scientific Instruments, 11*, 781–784.

Stoffregen, R. E., & Cygan, G. L. (1990). An experimental study of Na-K exchange between alunite and aqueous sulfate solutions. *American Mineralogist, 75*(1–2), 209–220.

Türkdönmez, O., & Bozcu, M. (2008). Etili (Çanakkale) güneyindeki plütonik ve volkanik kayaların petrografisi ve jeokimyası. *Geosound, 53*, 189–201.

Türkdönmez, O., & Bozcu, M. (2012). The geological, petrographical and engineering properties of rhyolitic tuffs (Çan Stone) in Çan-Etili Area (Çanakkale), NW Turkey: Their usage as building and covering stones. *Open Journal of Geology, 2*(1), 25–33.

Wade, C. E., McAvaney, S. O., & Gordon, G. A. (2014). Epithermal-style mineral textures, brecciation, veining and alteration, southern Gawler Ranges, SA. *Mathematics in Engineering Science and Aerospace Journal, 74*(3), 31–43.

White, D. E., Hutchinson, R. A., & Keith, T. E. C. (1988). The geology and remarkable thermal activity of Norris Geyser Basin, Yellowstone National Park, Wyoming. *Geological Survey Professional Paper, 1456*, 1–84.

Whitney, D. L., & Evans, B. W. (2010). Abbreviations for names of rock-forming minerals. *American Mineralogist, 95*(1), 185–187.

Yang, M., Liang, X., Ma, L., Huang, J., He, H., & Zhu, J. (2019). Adsorption of REEs on kaolinite and halloysite: A link to the REE distribution on clays in the weathering crust of granite. *Chemical Geology, 525*, 210–217.

Yiğit, Ö. (2012). A prospective sector in the Tethyan Metallogenic Belt: Geology and geochronology of mineral deposits in the Biga Peninsula, NW Turkey. *Ore Geology Reviews, 46*, 118–148.

Yılmaz, Y., & Karacık, Z. (2001). Geology of the northern side of the Gulf of Edremit and its tectonic significance for the development of the Aegean grabens. *Geodinamica Acta, 14*(1–3), 31–43.

Zattin, M., Okay, A. I., & Cavazza, W. (2005). Fission-track evidence for late Oligocene and mid-Miocene activity along the North Anatolian Fault in south-western Thrace. *Terra Nova, 17*(2), 95–101.

https://doi.org/10.1007/s42860-022-00214-4 Published online by Cambridge University Press